Characterization of Transport Regimes and the Polar Dome during Arctic Spring and Summer using in-situ Aircraft Measurements

Heiko Bozem[1], Peter Hoor[1], Daniel Kunkel[1], Franziska Köllner[1,2], Johannes Schneider[2],
Andreas Herber[3], Hannes Schulz[3], W. Richard Leaitch[4], Amir A. Aliabadi[5], Megan D. Willis[6,*],
Julia Burkart[6,**], and Jonathan P. D. Abbatt[6]

[1]Johannes Gutenberg University of Mainz, Institute for Atmospheric Physics, Mainz, Germany
[2]Particle Chemistry Department, Max Planck Institute for Chemistry, Mainz, Germany
[3]Alfred Wegener Institute Helmholtz Centre for Polar and Marine Research, Bremerhaven, Germany
[4]Environment and Climate Change Canada, Toronto, Canada
[5]School of Engineering, University of Guelph, Guelph, ON, Canada
[6]Department of Chemistry, University of Toronto, Toronto, Canada
*now at: Chemical Sciences Division, Lawrence Berkeley National Laboratory, Berkeley, California, USA
**now at: University of Vienna, Aerosol Physics & Environmental Physic, Vienna, Austria

Correspondence: Heiko Bozem (bozemh@uni-mainz.de)

Abstract. The springtime composition of the Arctic lower troposphere is to a large extent controlled by transport of mid-latitude air masses into the Arctic. In contrast, precipitation and natural sources play the most important role during summer. Within the Arctic region sloping isentropes create a transport barrier, known as the polar dome. The polar dome varies in space and time, and exhibits a strong influence on the transport of air masses from mid-latitudes; enhancing transport during winter and inhibiting transport during summer.

We analyzed aircraft based trace gas measurements in the Arctic from two NETCARE airborne field campaigns (July 2014 and April 2015) with the Alfred Wegener Institute Polar 6 aircraft, covering an area from Spitsbergen to Alaska ($134\,°W$ to $17\,°W$ and $68\,°N$ to $83\,°N$). Using these data we characterized transport regimes of mid-latitude air masses travelling to the high Arctic based on CO and CO_2 measurements as well as kinematic 10-day back trajectories. We found that dynamical isolation of the high Arctic lower troposphere leads to gradients of chemical tracers reflecting different local chemical lifetimes, sources and sinks. In particular, gradients of CO and CO_2 allowed for a trace gas based definition of the polar dome boundary for the two measurement periods, which showed pronounced seasonal differences. Rather than a sharp boundary, we derived a transition zone from both campaigns. In July 2014 the polar dome boundary was at $73.5\,°N$ latitude and $299 - 303.5\,K$ potential temperature. During April 2015 the polar dome boundary was on average located at $66 - 68.5\,°N$ and $283.5 - 287.5\,K$. Tracer-tracer scatter plots confirm different air mass properties inside and outside of the polar dome in both spring and summer.

Further, we explored the processes controlling the recent transport history of air masses within and outside the polar dome. Air masses within the spring-time polar dome mainly experienced diabatic cooling while travelling over cold surfaces. In contrast, air masses in the summertime polar dome were diabatically heated due to insolation. During both seasons air masses outside the polar dome slowly descended into the Arctic lower troposphere from above through radiative cooling. Ascent to the middle and upper troposphere mainly took place outside the Arctic, followed by a northward motion. Air masses inside and

outside the polar dome were also distinguished by different chemical composition of both trace gases and aerosol particles. We found that the fraction of amine containing particles, originating from marine biogenic sources, is enhanced inside the polar dome. In contrast, concentrations of refractory black carbon are highest outside the polar dome indicating remote pollution sources.

5   Synoptic-scale weather systems frequently disturb the transport barrier formed by the polar dome and foster exchange between air masses from mid-latitudes and polar regions. During the second phase of the NETCARE 2014 measurements a pronounced low pressure system south of Resolute Bay brought inflow from southern latitudes, which pushed the polar dome northward and significantly affected trace gas mixing ratios in the measurement region. Mean CO mixing ratios increased from 77.9 ± 2.5 ppbv to 84.9 ± 4.7 ppbv between these two regimes. At the same time CO_2 mixing ratios significantly decreased

10   from 398.16 ± 1.01 ppmv to 393.81 ± 2.25 ppmv. Our results demonstrate the utility of applying a tracer based diagnostic to determine the polar dome boundary for interpreting observations of atmospheric composition in the context of transport history.

1   Introduction

In recent decades the Arctic has undergone dramatic changes affecting sea ice, snow, permafrost, surface temperature, land,

15   and atmospheric circulation (IPCC, 2013). Rising temperatures, twice as fast as in the rest of the world, have led to a significant retreat of Arctic sea ice (Stroeve et al., 2012; Jeffries et al., 2013). In addition to reduced extent, the thickness of sea ice has continuously decreased (Lindsay and Schweiger, 2015).

Mid-latitude emissions in the Northern Hemisphere are still the main source region of atmospheric pollutants in the Arctic (Barrie, 1986; Koch and Hansen, 2005; Stohl, 2006; Sharma et al., 2013; Arnold et al., 2016). Several studies either based

20   on in-situ measurements or modelling reported enhanced pollution throughout the Arctic troposphere that is dominated by northern Eurasian sources in the lower troposphere and mid-latitude North America and Asia above (Sharma et al., 2006; Shindell et al., 2008; Fisher et al., 2010; Hirdman et al., 2010; Hecobian et al., 2011; Brock et al., 2011; Schmale et al., 2011; Sodemann et al., 2011; Stohl et al., 2013; Law et al., 2014; Monks et al., 2015; Willis et al., 2018). Roiger et al. (2011) even found Asian pollution in the lowermost stratosphere. However, local emissions in specific regions within the Arctic are already

25   important (Stohl et al., 2013; Law et al., 2014; Schmale et al., 2018) and might gain influence in the near future. Continuing retreat of Arctic sea ice will increase the accessibility of the Arctic, thus leading to a potential increase of emissions from local sources of pollutants like shipping (Eckhardt et al., 2013; Corbett et al., 2010; Melia et al., 2016) and oil and gas extraction (Peters et al., 2011). Resulting atmospheric pollutants, such as aerosol and tropospheric ozone, contribute to Arctic warming (Shindell and Faluvegi, 2009; AMAP, 2015).

30   Compared to other regions of the Northern Hemisphere, the faster pace of the rising surface and lower tropospheric temperatures in the Arctic is commonly known as Arctic amplification (Holland and Bitz, 2003; Screen and Simmonds, 2010). The interplay between different processes fosters feedback mechanisms that further amplify changes in the environment. The decrease in sea ice reduces the surface albedo and increases latent and sensible heat fluxes into the atmosphere which in turn

results in warmer surface temperatures relative to mid-latitudes (Robock, 1983; Hall, 2004; Winton, 2006). Furthermore, Pithan and Mauritsen (2014) reported that temperature feedbacks also play an important role for Arctic amplification. Arctic Amplification could further cause important changes in the mid-latitude circulation (Cohen et al., 2014; Pithan et al., 2018). Zonal winds might weaken and the Rossby wave amplitude is supposed to increase especially during the fall and winter months (Francis and Vavrus, 2012; Francis et al., 2017). Unusual warm sea surface temperatures and low sea ice concentrations in the Arctic have already caused atmospheric circulation anomalies in winter (Lee et al., 2015). As a result, transport pathways for aerosol and pollution into the Arctic will change due to the changing circulation pattern in association with Arctic amplification.

Transport into the Arctic and especially into the Arctic lower troposphere is possible along different pathways, depending on the source area of air masses and the time of the year (Klonecki, 2003; Stohl, 2006; Law and Stohl, 2007; AMAP, 2015). Stohl (2006) identified three major pathways, which significantly contribute to transport from major pollution sources into the Arctic lower troposphere. In the following paragraphs we discuss these pathways in turn.

1) Rapid low level transport followed by an uplift at the Arctic front at the location and time when the Arctic front is located far north. For this transport route uplift and potential precipitation occurs mostly north of $70\,^{\circ}$N, which allows significant deposition of aerosol and water-soluble pollutants in the Arctic. In Stohl (2006) they estimated a transport time of 4 days or less. Significant emissions only from densely populated regions in Europe can be transported into the high Arctic lower troposphere via this route, because major emission regions in North America and Asia are located south of the polar front. Note that the Arctic front and the polar front are geographically two distinct features. The Arctic front, which is most well defined during the summer months, is thought to develop due to strong differential heating between the cold Arctic ocean and adjacent ice and snow free land (Serreze et al., 2001; Crawford and Serreze, 2015). The Arctic front marks the southern boundary of the cold Arctic air mass that is separated from the less cold polar air mass further south. The polar front in contrast is the well known frontal zone separating warm mid-latitude and subtropical air masses from colder polar air masses. It is in general located further south compared to the Arctic front and displaced equatorward in summer and poleward in winter. In this baroclinic region characterized by strong horizontal temperature gradients, cyclones develop from an initial disturbance at the front. During the winter months the Arctic front can extend far south over the continents and can eventually be co-located or merge with the polar front.

2) Low level transport of already cold air masses into the polar dome, which is associated with further diabatic cooling during the transport time scale of 10-15 days. This pathway from European and high latitude Asian sources mainly occurs during winter, since transport over snow-covered regions (e.g. Siberia) is involved. Thus, strongly polluted air masses could be transported into the high Arctic lower troposphere. This transport pathway is negligible during the summer months when the surface in Eurasia is a net source of heat (Klonecki, 2003).

3) Fast uplift mainly due to convection in southern mid-latitudes, followed by high altitude transport in northerly directions. Radiative cooling eventually leads to a slow descent into the polar dome area after air masses have arrived in the high Arctic. Being less frequent from Europe, this transport pathway is most prevalent from North America and East Asia. In contrast to the other two transport pathways, scavenging processes can occur during the strong ascent in mid-latitudes which can lead to a significant washout of aerosol and soluble pollutants outside the Arctic.

The high Arctic lower troposphere is in general quite well isolated from the rest of the Arctic by a transport barrier referred to as the polar dome. The polar dome is formed by sloping isentropes, the isolines of potential temperature Θ, as a result of radiative cooling in the high Arctic, especially during the winter months without sunlight (Barrie, 1986; Klonecki, 2003; Stohl, 2006). Air masses preferably maintain near constant potential temperatures during transport, since atmospheric circulation can be well described by adiabatic motions in the absence of diabatic processes related to clouds, radiation and turbulence. The potential temperature is low within the polar dome area and thus only air masses that have experienced diabatic cooling are able to enter the polar dome through the pathways discussed above (Stohl, 2006). As a consequence, the "Arctic haze" phenomenon is mainly fed by northern Eurasian pollution sources as those air masses are cold enough to enter the high Arctic lower troposphere (Carlson, 1981; Rahn, 1981; Raatz, 1985; Iversen, 1984; Barrie, 1986; Brock et al., 1990; Dreiling and Friederich, 1997). Already known for decades, Arctic haze has again gained attention at the beginning of the 21st century, triggered by the role of black carbon (BC) in Arctic climate change (Flanner et al., 2007; Hansen and Nazarenko, 2004; Law and Stohl, 2007; McConnell et al., 2007; Quinn et al., 2008; Shindell and Faluvegi, 2009). Pollution originating from outside the Arctic is transported into the high Arctic lower troposphere during the winter months and the lack of sunlight allows for a build-up of aerosol particles and gaseous pollutants. When temperatures during the winter months become extremely low near the surface, the Arctic lower troposphere is thermally very stably stratified with surface based inversions that can persist for several days (Bradley et al., 1992). Turbulent exchange and hence dry deposition is reduced under these conditions. Furthermore, the lower troposphere is extremely dry, preventing scavenging of aerosol and gaseous pollutants by wet deposition. At the spring-time peak, Arctic haze is often visible as layers of brownish haze affecting the radiation budget of the Arctic lower troposphere and also contributing to contamination of the Arctic environment. During the transition to pristine summer conditions Arctic haze declines due to efficient aerosol scavenging in mid-latitudes during convective uplift. Anthropogenic aerosol is further reduced by frequent precipitation of low intensity within the Arctic lower troposphere (Barrie, 1986; Browse et al., 2012; Garrett et al., 2010).

In general, the polar dome boundary, acting as a transport barrier for warmer mid-latitude air masses, is variable in time and space. Synoptic disturbances can lead to a shift of the polar dome boundary or perturb the transport barrier, and foster exchange with mid-latitude air that can alter the composition of the lower Arctic troposphere. A distinct definition of the polar dome boundary location is crucial to understand and quantify effects on atmospheric composition. Although the polar dome has been known for decades, only very few specific definitions of the polar dome boundary have been described in the literature. In early studies of Arctic haze, Carlson (1981) or Raatz (1985) identified the polar front as a transport barrier decoupling the Arctic from influence of mid-latitude air masses. More recent studies used the location of the more northern Arctic front as a marker for the polar dome as a transport barrier (Klonecki, 2003; Stohl, 2006). Jiao and Flanner (2016) used the maximum zonal mean latitudinal gradient of $500\,\mathrm{hPa}$ geopotential height in the Northern Hemisphere. One of the drawbacks of the latter approach is the missing definition at lower altitudes.

The polar dome is well isolated from the surrounding troposphere, which lead to long residence times of air masses within the polar dome. Anthropogenic tracers like CO and CO_2 show temporal changes within days to weeks due to changes in emissions and the source strength of these species. Furthermore the distribution of sources and sinks as well as the efficiency
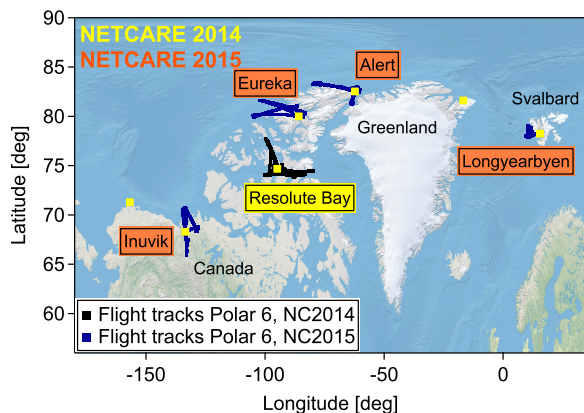
Figure 1. Compilation of of research flight tracks during two NETCARE airborne field campaigns in July 2014 and April 2015.

of removal processes for both species is different within the Arctic and at mid-latitudes, leading to latitudinal gradients for both species. Given the isolation created by the polar dome, we expect measurable gradients in tracer species across its boundary. In this study we use gradients of CO and CO_2 to derive a tracer based diagnostic to identify the polar dome boundary location. The basis for this analysis are two airborne field campaigns: NETCARE 2014 in July and NETCARE 2015 in April (Section

5 2, 3, 4), covering late spring to summer. Despite focussing on only these specific time periods, this study is the first attempt to define the polar dome boundary based on airborne trace gas gradients (Section 5). We use our trace gas definition of the polar dome boundary to analyze transport history and atmospheric composition within and outside the polar dome.

2 The NETCARE project

The NETCARE project (Network on Climate and Aerosols: Addressing Key Uncertainties in Remote Canadian Environments,

10 http://www.netcare-project.ca) is configured around four research activities addressing key uncertainties in the field of Arctic aerosol climate research (Abbatt et al., 2019). Within this framework two aircraft based measurement campaigns were performed in the high Arctic. The main objectives of both campaigns were to study aerosol-cloud interactions as well as to characterize local and remote sources for pollution within the high Arctic lower troposphere in summer 2014 (July) and spring 2015 (April). Figure 1 shows a compilation of flight tracks for the two airborne research activities named NETCARE 2014 and

15 NETCARE 2015.

The first project was performed from July 4th to July 21st, 2014 with the Polar 6 aircraft based in Resolute Bay, Nunavut, Canada (e.g. Aliabadi et al. (2016); Leaitch et al. (2016); Willis et al. (2016, 2017); Burkart et al. (2017); Köllner et al. (2017)). In total 11 research flights, each between 4-6 hours long, covered two main areas, Lancaster Sound east of Resolute Bay and north of Resolute Bay where two polynyas were located. During the last part of the campaign, July 19th to July 21st, a special

20 research focus was on ship emission measurements (Aliabadi et al., 2016).

Table 1. Location and coordinates for the different stations from which measurement flights were performed during the two NETCARE airborne projects in July 2014 and April 2015. Additionally the time at the station and the number of research flights are given.

	Location	Coordinates	Date	Flights
NETCARE 2014	Resolute Bay	74.7 °N, 95.0 °W	July 4th to July 21st	11
NETCARE 2015	Longyearbyen	78.2 °N, 15.5 °E	April 5th	1
	Alert	82.5 °N, 62.3 °W	April 7th to April 9th	4
	Eureka	80.0 °N, 85.8 °W	April 11th to April 17th	2
	Inuvik	68.3 °N, 133.5 °W	April 20th to April 21st	3

The second aircraft project took place in April, 2015. We performed pan-Arctic measurements throughout the European and Canadian Arctic (see Fig. 1). This campaign was a joint NETCARE and PAMARCMiP (https://www.awi.de/en/science/climate-sciences/sea-ice-physics/projects/netcare-arctic-study-of-short-lived-climate-pollutants/pamarcmip-2015.html) project, which will be referred to as "NETCARE 2015" throughout this paper (e.g. Libois et al. (2016); Willis et al. (2019); Schulz et al. (2019)). During 10 research flights, each 4-6 hours long, we specifically focused on a better understanding of aerosol transport into the Arctic in early spring and its influence on ice cloud formation. More details of the different base stations can be found in Tab. 1. Multiple vertical profiles from the lowest possible altitude of 60 m up to 6000 m were performed to study the vertical distribution of aerosol particles and trace gases.

3 Methodology

3.1 Measurement platform

Airborne measurements were performed using the Polar 6 aircraft of the Alfred Wegener Institute Helmholtz Center for Polar and Marine Research, Bremerhaven, Germany. Polar 6 is a DC 3 aircraft converted to a Basler BT67 (Herber et al., 2008) and modified for operation in cold and harsh environments. The aircraft has a non-pressurized cabin, however flights up to an altitude of 6 km were regularly performed during the 2014 and 2015 campaigns. The typical survey speed of the aircraft is 120 kts ($\cong 60\,\mathrm{m\,s^{-1}}$) with ascent and descent rates of $150 - 300\,\mathrm{m\,min^{-1}}$ during vertical profiles.

3.2 Instrumentation

Meteorological and aircraft altitude data for Polar 6 are provided by the AIMMS-20 instrument. The instrument was designed and manufactured by Aventech Research Inc., Barrie, Ontario, Canada. It includes the Air Data Probe (ADP) that reports the three-dimensional, aircraft-relative flow vector consisting of true air speed, angle-of-attack and sideslip. In the rear section of the instrument, temperature and relative humidity sensors are located providing data with an accuracy of $0.30\,^{\circ}\mathrm{C}$ for temperature measurements and $2.0\,\%$ for humidity measurements, respectively. A GPS module provided the aircraft 3-D position and inertial velocity. Horizontal and vertical wind speeds were measured with accuracies of 0.50 and $0.75\,\mathrm{m\,s^{-1}}$, respectively. All

data were internally sampled with 200 Hz resolution and for further analysis averaged to 1 Hz resolution. From the AIMMS-20 data set, temperature and pressure data are used throughout this study. The instrumentation for aerosol and cloud droplets as well as upwelling radiance measurements are described in detail in Leaitch et al. (2016); Willis et al. (2016); Burkart et al. (2017); Aliabadi et al. (2016); Libois et al. (2016) and Schulz et al. (2019).

5   CO was measured with an Aerolaser ultra fast carbon monoxide (CO) monitor model AL 5002 based on VUV-fluorimetry, using the excitation of CO at 150 nm. Details on the measurement principle can be found in Gerbig et al. (1999) or Scharffe et al. (2012). The instrument was modified for applying in-situ calibrations during in-flight operations. We performed these regular in-situ calibrations on a 15 to 30 min time interval during measurement flights using a NIST traceable calibration gas with a known CO concentration at atmospheric levels as well as zero measurements. Calibrations and zero measurements

10   account for instrument drifts. CO data achieved a precision ($1\,\sigma$, 1 Hz) of 2.2 ppbv during NETCARE 2014 and 1.5 ppbv during NETCARE 2015. We calculated the stability of the instrument to 4.1 ppbv and 1.7 ppbv, respectively, before applying the post flight data correction. Stability is a measure of reproducibility and based on the mean drift between two subsequent calibrations which were performed during flights. Stability is mainly affected by temperature variations. These instrumental drifts are corrected after the flights assuming linear drift. Hence, the total uncertainty of 4.7 ppbv relative to the working

15   standard for NETCARE 2014 and 2.3 ppbv for NETCARE 2015 can be regarded as an upper limit.

     CO_2 was measured with a LI-7200 closed CO_2/H_2O Analyzer from LI-COR Biosciences GmbH. The instrument simultaneously also measures water vapour, which is used for CO_2-H_2O-interference corrections. The measurement principle is based on an optical source emitting infrared light through a chopper filter wheel and the enclosed sample path to a temperature controlled lead selenide detector. By using the ratio of absorption by carbon dioxide in the sample path to a reference, the

20   density of the gases and thus the mixing ratio can be calculated. The instrument itself was mounted in a 19", 3 HE rack mount including additional components for flow control and in-situ calibrations during in-flight operations. As for the CO measurements, we performed calibrations on a regular time interval of 15 to 30 minutes using a NIST traceable calibration gas with a known CO_2 concentration at atmospheric levels and a water vapour concentration close to zero. CO_2 data during NETCARE 2014 achieved a precision ($1\,\sigma$, 1 Hz) of 0.02 ppmv and 0.05 ppmv during NETCARE 2015. Using the same methodology as

25   for CO, we calculated the stability of the instrument to 0.76 ppmv for NETCARE 2014 and 1.72 ppmv for NETCARE 2015, before applying the post flight data correction. The total uncertainty relative to the working standard thus amounts to 0.76 ppmv for NETCARE 2014 and 1.72 ppmv for NETCARE 2015. The uncertainty for the measurement of H_2O is 18.5 ppmv or 2.5 %, whichever is greater.

3.3   LAGRANTO backward trajectories

30   We used the Lagrangian analysis tool (LAGRANTO) (Wernli and Davies, 1997; Sprenger and Wernli, 2015) to determine the origin of air masses that were sampled. LAGRANTO trajectories were calculated based on operational analysis data from the European Centre of Medium-Range Weather Forecasts (ECMWF). This data has a horizontal grid spacing of $0.5\,°$ with 137 hybrid sigma-pressure levels in the vertical from the surface up to 0.01 hPa. Trajectories were initialized every 10 s from coordinates along individual research flights and calculated 10 days back in time. The location of the individual trajectory

is available at a 1 h time interval. Different variables of atmospheric state were simulated along the trajectory (temperature, potential temperature, potential vorticity, specific humidity, cloud water and cloud ice water content, Richardson number and equivalent potential temperature).

To account for the latitudinal transport history of the air parcels we calculated the median latitude along the trajectories. We used this as a proxy for the most representative position during the last 10 days associated with the respective values of CO and CO_2. To account for diabatic descent occurring during transport we calculated the maximum potential temperature. Both parameters are used in Sec. 5.2 for the analysis of the polar dome boundary. As a measure for the uncertainty of the temperature along the trajectory we calculated the median difference between temperatures measured in-situ on the aircraft and the corresponding temperatures interpolated to the initialisation point of the trajectory along the flight track based on analysis data. For the measurements in July 2014 the median difference is $0.31\,°C$ (interquartile range: $-0.71 - 1.72\,°C$). For the April 2015 measurements, the respective median difference is $1.50\,°C$ (interquartile range: $0.69 - 2.14\,°C$).

4 Meteorological Overview

4.1 NETCARE 2014

The meteorological situation can be separated into two different meteorological regimes (see Fig. 2). During the first phase (July 4th to July 12th) the boundary layer was capped at low altitudes by a distinct temperature inversion leading to a stable stratification of the lower troposphere. The prevailing influence of a high pressure system provided ideal conditions for aircraft based measurements with mainly clear sky, only few or scattered clouds and low wind speed. Beginning July 13th Resolute Bay was influenced by a low pressure system located to the west above the Beaufort Sea. This system eventually passed Resolute Bay two days later. Increased humidity, precipitation and fog characterized the local weather and prevented Polar 6 from flying until July 17th. The last flights of the campaign were performed between July 19th and July 21st when a pronounced low pressure system south of Resolute Bay and centred around King William Island influenced the measurement region (see Fig. 2b). Increased wind speeds, mostly mid to high level clouds and precipitation resulted from the inflow of warm air from more southern latitudes. Furthermore, this situation was favourable for mid-latitude air masses being advected to the measurement region potentially affecting concentrations of trace gases and aerosol particles.

4.2 NETCARE 2015

The aircraft were based at four different locations, namely Longyearbyen (Norway), Alert, Eureka (both Nunavut, Canada) and Inuvik (Northwest Territories, Canada), allowing for a wider coverage of the entire Arctic. Figure 3 shows mean geopotential height at $850\,hPa$ over the time interval of the measurements in the respective region. At the time of the first flight of the campaign in Longyearbyen (April 5th, see Fig. 3a), Spitsbergen was under a quite stable high pressure influence with almost no clouds and only weak winds. During the measurements in Alert the meteorological situation was dominated by a pool of cold air centred above Ellesmere Island to the south-west of Alert. A cyclonic flow was established around this cold air guiding
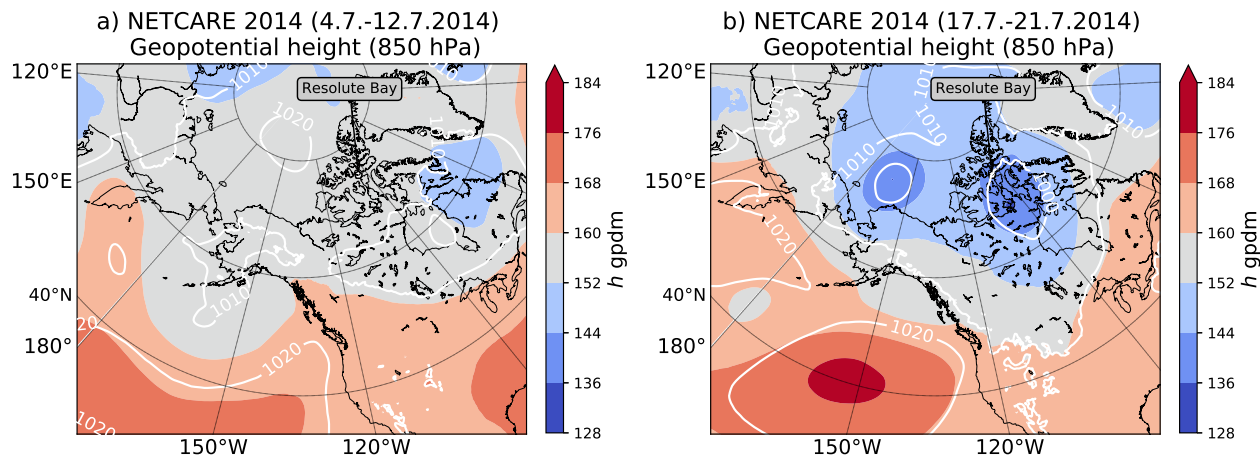
Figure 2. Mean geopotential height on $850\,\mathrm{hPa}$ in geopotential decameter (gpdm) for the period from July 4th 2014 to July 12th 2014 (a) and for the period from July 17th 2014 to July 21st 2014 (b).

low pressure systems around the cold pool and thus preventing mid-latitude air masses from influencing the high Arctic lower troposphere. Stable conditions with almost clear sky facilitated airborne measurements on 4 research flights between April 7th and April 9th during this period (see Fig. 3b). After the transfer to Eureka on April 10th two research flights were performed in almost the same meteorological conditions as in Alert. When the surface low started moving south over Baffin Bay from
5   April 13th onward (see Fig. 3c) strong northerly and north-easterly winds in the lower troposphere influenced the measurement regions. The warmer flow was guided from southern areas over open water around the low pressure centre and was associated with moisture transport to the land leading to cloud formation and fog, which impeded research flights out of Eureka. In the following days a low pressure system started intensifying north of Greenland and maintained the low level moist northerly flow. The last flights of the campaign were conducted in Inuvik between April 20th and April 21st. After the ferry from Eureka to
10   Inuvik on April 17th and 18th high pressure influence was prevalent in Inuvik. At the time of the research flights a low pressure system located over Alaska fostered a southerly and south easterly flow into the Inuvik area, favourable for mid-latitude air masses to enter the measurement region (see Fig. 3d). A detailed description of the air mass history corresponding to the meteorological situation is given in the supplementary material (Fig. S1 and S2).

5   Results

15   ### 5.1   Trace gas observations

Based on the meteorological situation and transport regimes discussed above, we expect a significant influence of air mass history on the mixing ratios of CO and CO_2. Both species show latitudinal and vertical gradients (see Fig. 4) and both are
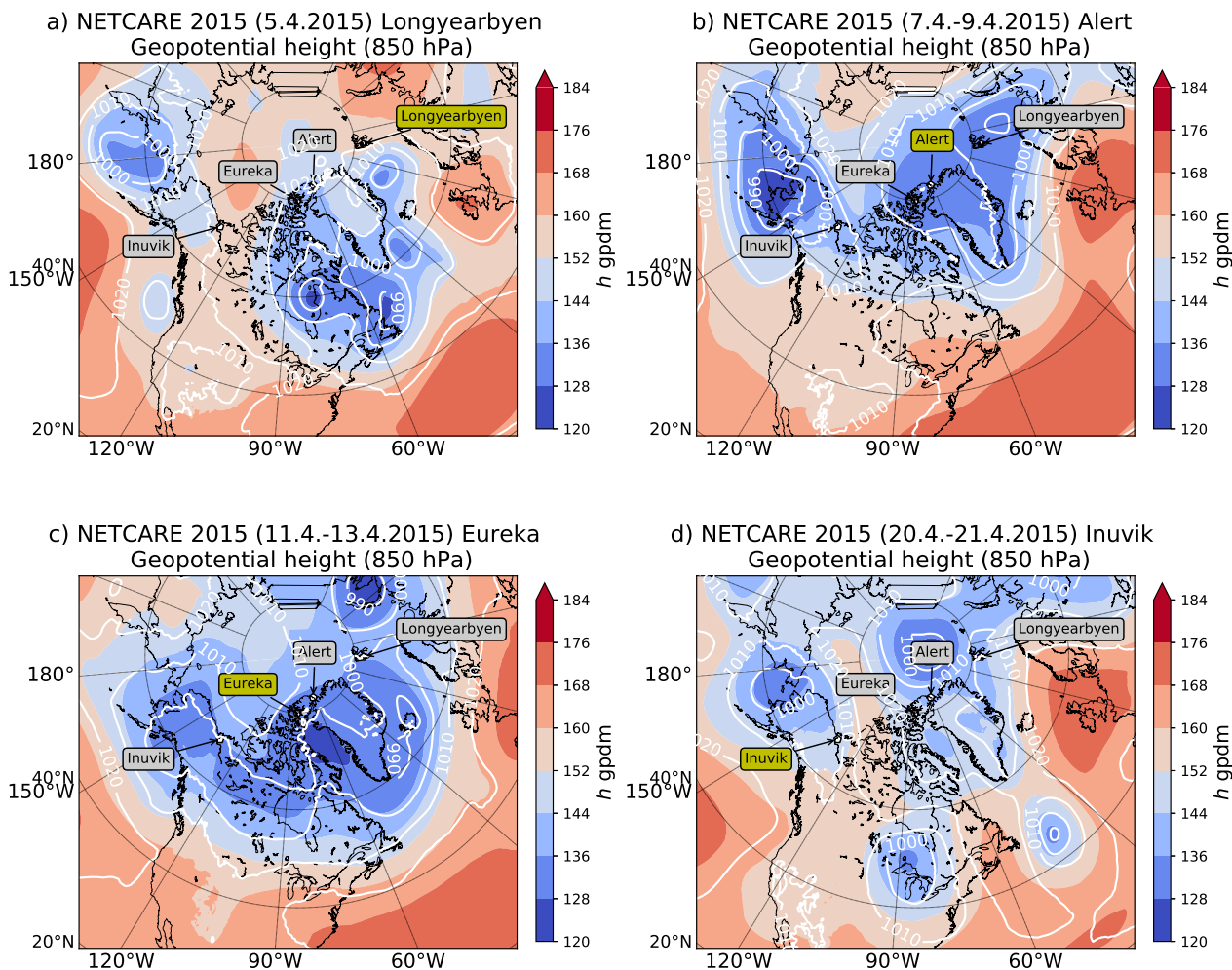
Figure 3. Mean geopotential height on $850\,\mathrm{hPa}$ in geopotential decameter (gpdm) from April 5th 2015 (a), from April 7th 2015 to April 9th 2015 (b), from April 11th 2015 to April 13th 2015 (c) and from April 20th 2015 to April 21st 2015 (d). Our flight location for each time period is marked in yellow.

affected by anthropogenic pollution, making them ideally suited for identification of pollution events affecting the Arctic background. Our aircraft based measurements of CO and CO_2 are in very good agreement with ground based observations (see Fig. 4). In April 2015 trace gas levels are in general higher compared to July 2014. The observed change in trace gas levels between spring and summer reflects the typical seasonal cycle of these two species in the Arctic.

5   The high Arctic CO seasonal cycle shows a maximum in late winter/early spring and a minimum during late summer. This seasonal maximum reflects the transport of anthropogenic pollutants - mainly from fossil fuel burning - from northern Europe and Siberia into the high Arctic lower troposphere during winter (Klonecki, 2003; Stohl, 2006). Since photochemically
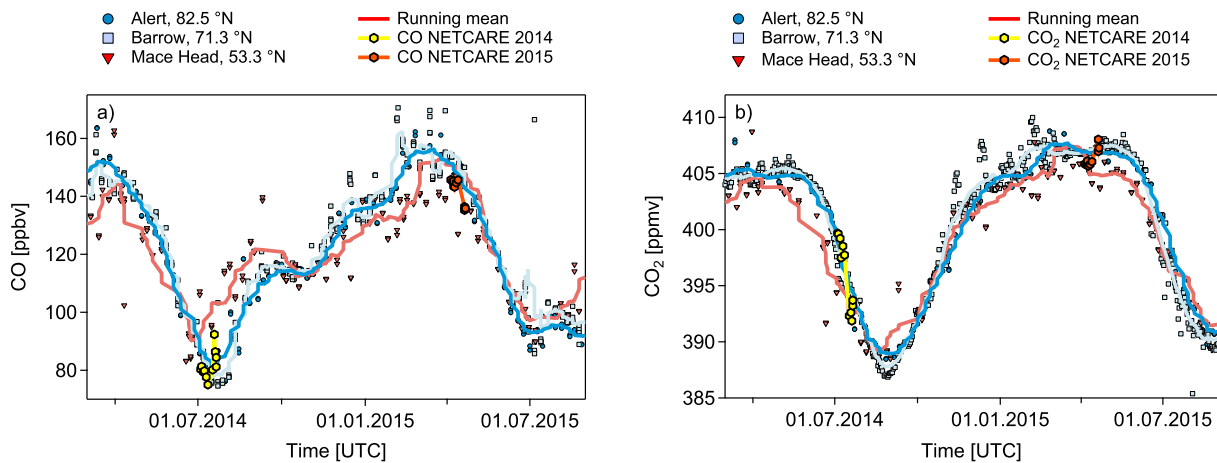
Figure 4. CO (Dlugokencky et al., 2018) (a) and CO_2 (Petron et al., 2018) (b) seasonal cycle based on NOAA ground based measurements in Alert (Canada), Barrow (Alaska) and Mace Head (Ireland) for the years 2014 and 2015. Running means are shown for the respective station data (symbols). Mean aircraft data for altitudes lower than 200 m for individual flights are overlaid. Error bars (yellow and orange shading) for the aircraft data are too small to be visible. NETCARE 2014 data are in yellow and NETCARE 2015 data are in orange.

produced OH is absent during wintertime due to the lack of sunlight, CO in the high Arctic has no significant sink which results in a longer chemical lifetime on the order of months. Hence, CO increases over the course of the winter, in particular within the polar dome (Novelli et al., 1998; Engvall et al., 2008). As soon as sunlight returns during late February and early March there is a sharp transition between 24 h polar night and 24 h polar day. The increasing concentration of OH leads to increased oxidation

5 of CO and a shorter lifetime on the order of weeks (Dianov-Klokov and Yurganov, 1989; Holloway et al., 2000). During the transition from spring to summer (April to June) photochemical activity in the Arctic and smaller mid-latitude emissions of CO lead to decreasing CO in the Arctic until a minimum is reached at the end of the summer (Barrie, 1986; Klonecki, 2003; Engvall et al., 2008).

The CO_2 seasonal cycle in the northern hemisphere is mainly controlled by carbon uptake and release processes of the

10 biosphere (Keeling et al., 1996; Forkel et al., 2016). Whereas during the summer months the CO_2 seasonal cycle reaches its minimum due to photosynthetic carbon uptake by vegetation, respiration of the biosphere is prevalent during wintertime. Particularly in Arctic winter, the absence of sunlight allows for a build-up of CO_2 concentrations. However, meridional CO_2 transport into the high Arctic by synoptic weather disturbances plays a critical role for the seasonal cycle and dominates over local atmosphere-biosphere fluxes (Fung et al., 1983; Parazoo et al., 2011; Barnes et al., 2016). As a result, the synoptic eddy

15 driven meridional transport reduces the seasonal cycle in mid-latitudes and amplifies it in polar regions, leading to a meridional CO_2 gradient (Parazoo et al., 2011).
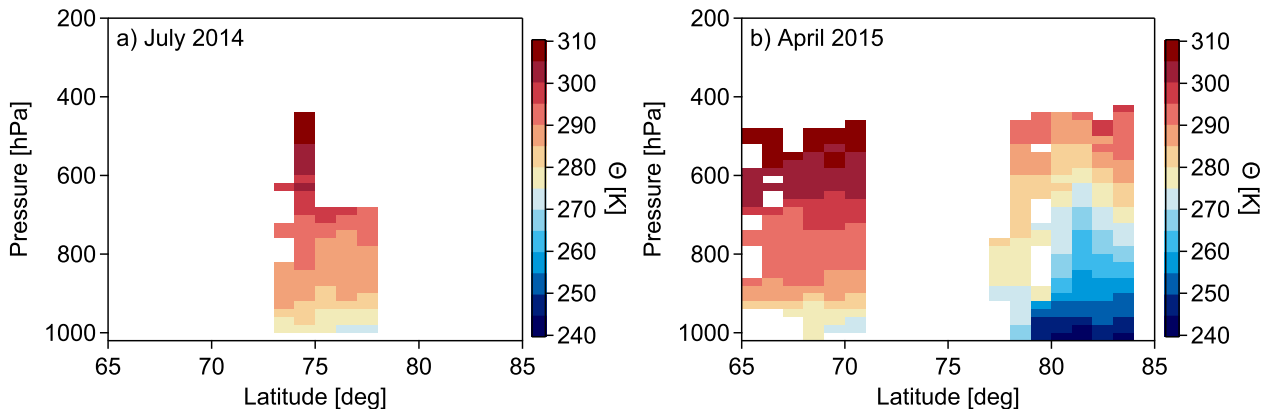
Figure 5. Potential temperature Θ as a function of latitude and pressure binned in steps of $1°$ latitude and $20\,\mathrm{hPa}$ pressure for July 2014 (a) and April 2015 (b). Note the dome like structure during April 2015 (NETCARE 2015) which is virtually absent for the Resolute Bay data during July 2014 (NETCARE 2014).

5.2 The polar dome location

The polar dome can be conceptualized vertically as the region below upward sloping isentropes, and horizontally as the region north of where low-valued isentrops intersect with the surface. Figure 5 shows the observed potential temperature (Θ) distribution as a zonal mean for the respective campaigns. Potential temperature was calculated from temperature and pressure

5 measurements on board the Polar 6 aircraft. A dome-like structure of the isentropes is visible for April 2015 (NETCARE 2015). Minimum potential temperatures lower than $275\,\mathrm{K}$ were only present in the high Arctic lower troposphere north of $70°\mathrm{N}$. In contrast, a dome-like structure is hardly visible for July 2014 (NETCARE 2014). Only below $950\,\mathrm{hPa}$ and north of $75°\mathrm{N}$ Θ values of $275\,\mathrm{K}$ were observed. Our observations are in agreement with previous studies which showed that during the summer months the extent of the polar dome is much smaller compared to the winter time (Klonecki, 2003; Stohl, 2006;

10 Jiao and Flanner, 2016).

If we now use potential temperature as the vertical coordinate, air masses within the polar dome associated with the coldest potential temperatures should separate from other regions. This separation is evident in Fig. 6, particularly for the April 2015 measurements (b). The colour code in Figs. 6a and b represents the average CO background mixing ratio calculated from all data points within the respective bin interval. In our analysis of the polar dome we only use background trace gas mixing ratios.

15 We exclude polluted air masses, if the mean background CO mixing ratio is exceeded by 2 standard deviations. In April 2015 (Fig. 6b) northernmost latitudes exhibited the largest CO values of 140-150 ppbv for potential temperatures lower than $275\,\mathrm{K}$. At higher isentropes typical CO values range from 100-135 ppbv. At these higher potential temperatures, the larger variability of CO mixing ratios indicates different source regions contributing to the observations, which is in particular observed for the lower latitudes. In the distribution for the summer campaign (Fig. 6a) a region of rather uniform low CO is evident north of

20 $75°\mathrm{N}$ and below $290\,\mathrm{K}$. Mixing ratios south of $75°\mathrm{N}$ and above $290\,\mathrm{K}$ tended to be more variable and in general larger than
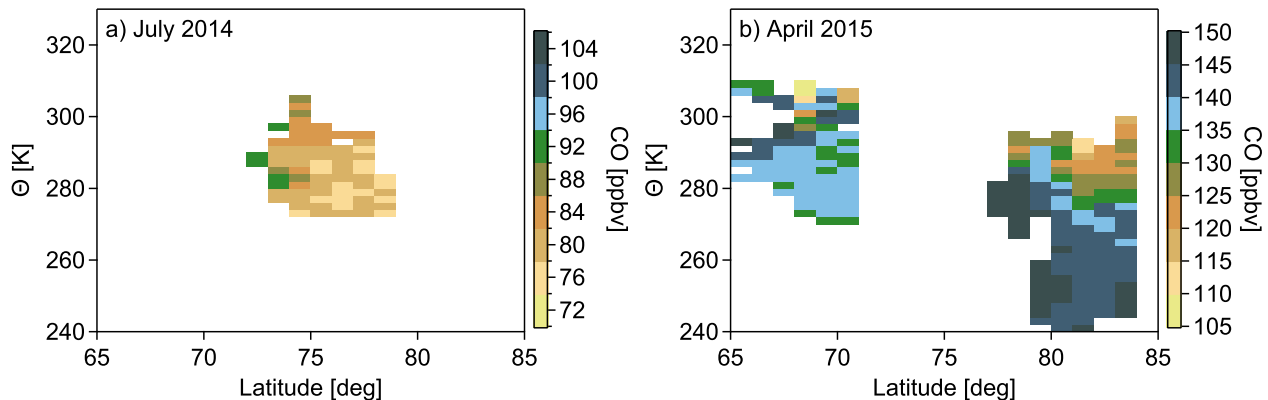
Figure 6. CO distribution binned by latitude and potential temperature for July 2014 (a) and April 2015 (b). The colour code represents the average CO mixing ratio calculated from all data points in the respective $1°$ latitude and $2\,K$ bin interval. Note that only background mixing ratios are shown now. Polluted air masses are identified and filtered when the average background distribution is exceeded by 2σ.

within the the more northern region. Again, the increased variability results from different air mass origins associated with different levels of CO. In both measurement campaigns, we observed a distinct transition between the northernmost lower troposphere and regions with lower latitudes and larger potential temperatures. This transition indicates a transport barrier for air masses to reach the high Arctic lower troposphere. We hypothesize that those regions north of $75°N$ showing the lowest CO mixing ratios during July 2014, and the largest during April 2015, represent the polar dome whereas the rest of the measurements were collected outside the polar dome.

The trace gas distribution in Fig. 6 only shows a snapshot of the actual situation at the time and the location of the measurement. We used ten day backward trajectories to take into account different transport pathways to the Arctic and the residence times of air masses inside the polar dome area, which is likely higher than residence times in areas outside the polar dome. We display the CO and CO_2 distribution in a maximum potential temperature versus median latitude coordinate system. Maximum potential temperature and median latitude were derived along every individual trajectory. Median latitude allows for a separation between high Arctic air masses and air masses from mid-latitudes. Air parcels isolated in the polar dome region should stay at high median latitudes whereas air masses extending over a larger meridional distance show a more southern median latitude. Maximum potential temperature further allow us to account for diabatic descent of air masses during transport. In the maximum potential temperature vs. median latitude coordinate system those air masses inside the polar dome region exhibit the lowest maximum potential temperatures and at the same time largest median latitudes, and thus separate from air masses outside the polar dome. Furthermore, the polar dome is dynamically well isolated from the surrounding troposphere as discussed earlier. Hence, air parcels inside the polar dome are in general not affected by strong mid-latitude CO sources and should show a relatively small CO variability. Therefore, we remapped the CO data to the median latitude and maximum potential temperature along the trajectory to identify transport regimes and the effect of the transport barrier at the polar dome (see Figs. 7a and c). The majority of trajectories with relatively low CO mixing ratios are confined by the $305\,K$ isentrope
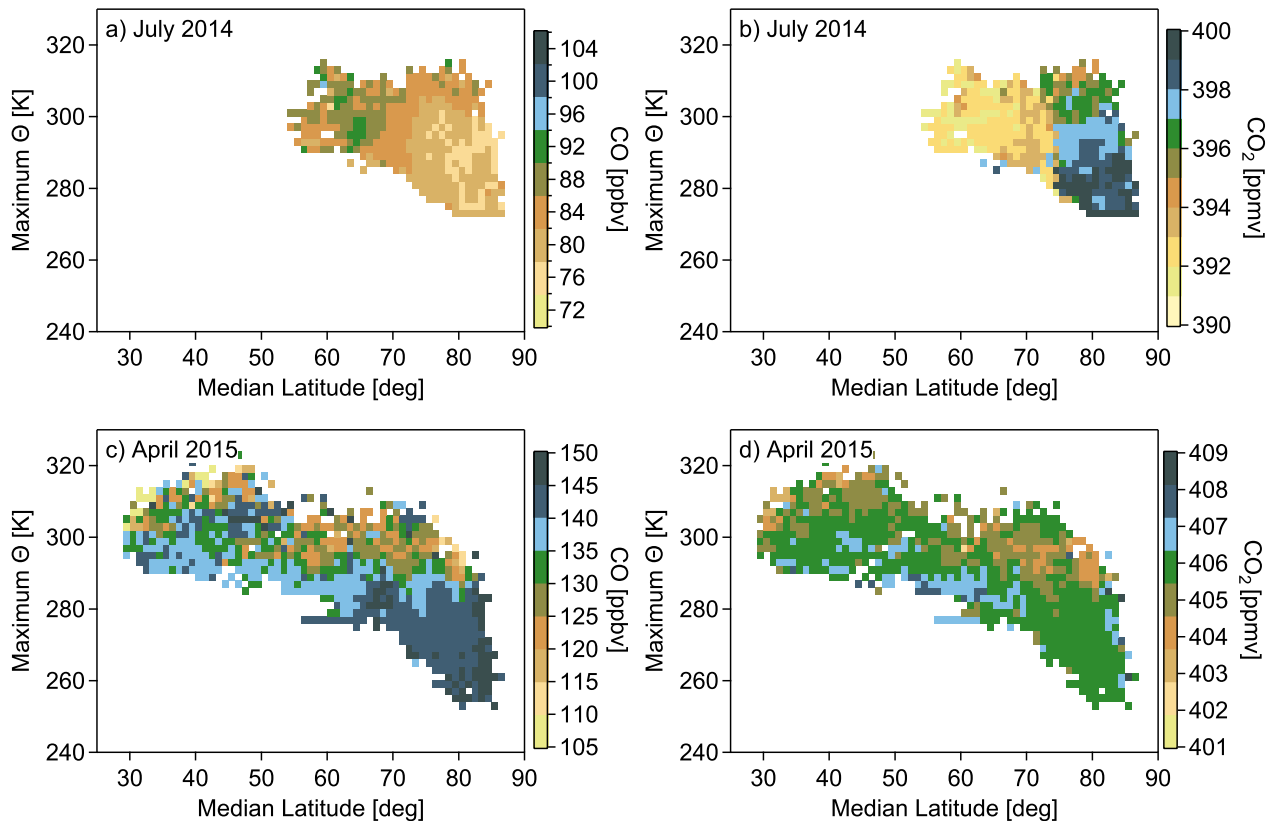
Figure 7. (a-d): Trace gas distribution in the maximum potential temperature and median latitude coordinate system. The median and maximum values were derived from every 10-day-trajectory calculated along the flight track. The colour code is representative for the average CO (CO_2) value calculated from all data points within one bin interval. The trace gas mixing ratio is the measured value which is assumed to stay constant along the respective trajectory for each measured data point every 10 s.

and $70\,°N$ as evident in Fig. 7a for July 2014. For April 2015 (Fig. 7c) an area with relatively higher CO is located north of a latitude of $65\,°N$ and below a potential temperature of around $280\,K$. These findings are supported by the CO_2 distribution in the same coordinate system displayed in Figs. 7b and d, which show similar boundaries. Hence, gradients of CO and CO_2 establish at these boundaries. In this study these chemical gradients are used to derive a tracer based definition of the polar dome boundary for the two NETCARE measurement campaigns during July 2014 and April 2015. Next, we determine the location of the polar dome boundary based on trace gas gradients.

Trace gas gradients

In July 2014 both CO and CO_2 show a latitudinal gradient across the isentropes for maximum potential temperature levels of $\Theta < 305\,K$ (see Fig. 7a and b). In particular, CO_2 shows a strong increase from values around $393\,ppmv$ to $398\,ppmv$ toward
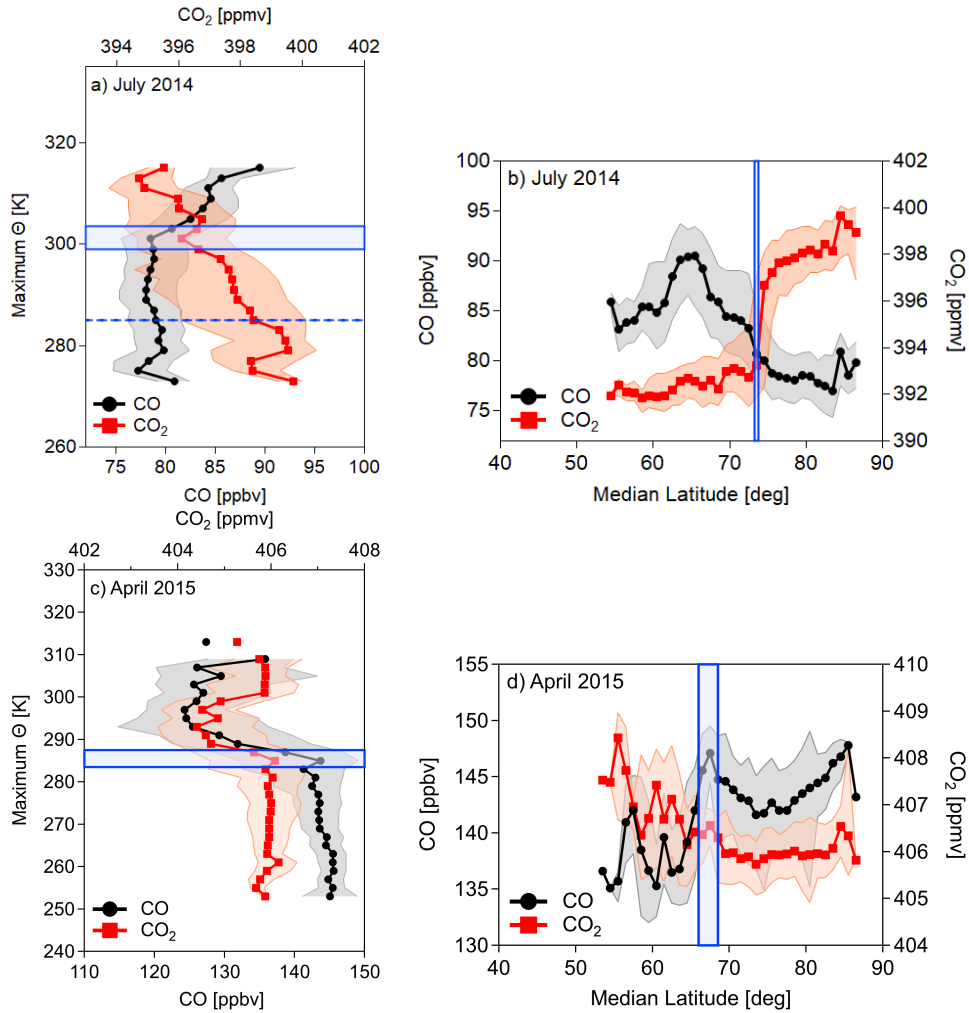
Figure 8. Medians of CO and CO_2 as a function of median trajectory latitude and maximum trajectory potential temperature (details see text). Median values for the vertical profiles were only calculated north of $75\,°N$ for July 2014 (a) and north of $65\,°N$ for April 2015 (c) because latitudinal gradients indicate a dome boundary north of these median latitudes. At lower latitudes transport and mixing homogenize these gradients (see Fig. 7). For both NETCARE campaigns the median horizontal values were derived only below $300\,K$ (b and d). The blue bar marks the latitude and the potential temperature interval of the strongest change in the tracer mixing ratio, which is interpreted as the transition zone of the polar dome boundary. The shaded area in all figures represents the $1\,\sigma$ standard deviation.

high latitudes in the median latitude range of $70\,°N$ to $75\,°N$. For CO, a decrease from about $83\,ppbv$ to $78\,ppbv$ in this latitude range is also evident. In contrast to CO_2 the large variability of CO at lower median latitudes reflects a larger variability of potential source regions, which in turn partly masks the CO gradient. Above $305\,K$ trace gas gradients are weak or absent, indicating rapid isentropic mixing from lower latitudes. We now calculate isentropic trace gas gradients in layers of $2\,K$ for the maximum potential temperature as the vertical coordinate in Fig. 7 to derive the horizontal polar dome boundary. Hence,
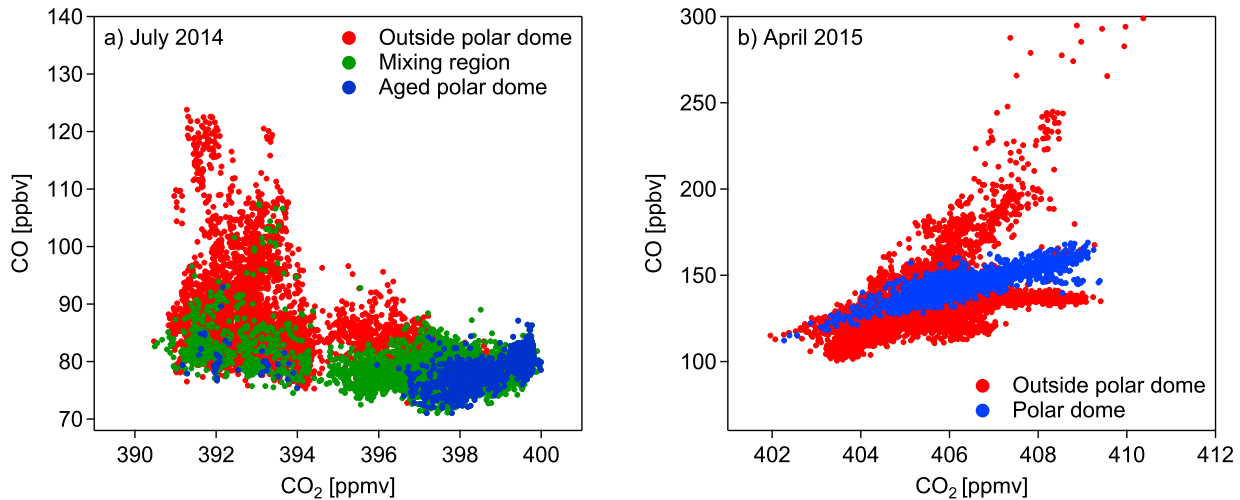
Figure 9. (a): Tracer-tracer scatter plot of all data points (background + pollution plumes) within the aged polar dome (blue), the mixing region (green) and outside the polar dome (red) for July 2014. (b): Tracer-tracer scatter plot of all data points (background + pollution plumes) within (blue) and outside (red) the polar dome for April 2015. To separate the different regions the tracer derived polar dome boundaries are used. Boundary values for each region are summarized in Tab. 2

for every 2 K altitude interval we determine the latitude of the strongest trace gas gradient. Below 305 K isentropic trace gas gradients maximize around 73 °N. We finally use the median of these maximum gradient latitudes to define the polar dome boundary. If we derive a different median value for the maximum gradient for each of the two tracer species, we consider this difference as the range of the polar dome boundary which can be interpreted as a transition zone rather than a sharp boundary.

5   For July 2014 the average horizontal polar dome boundary is a sharp transition at 73.5 °N (blue bar in Fig. 8b). The interquartile range denotes to 72.5 °N - 77 °N.

The strongest vertical gradients of CO and CO_2 were determined at maximum potential temperature values of 299 - 303.5 K (blue bar in Fig. 8a; interquartile range: 297 to 304.5 K). These values for the upper polar dome boundary are relatively high given a surface value of potential temperature of typically 280 K in summer. A close inspection of the CO_2 distribution north

10   of 73.5 °N (Fig. 7b) reveals two layers in the high Arctic separated at approximately 285 K. The vertical profile of CO_2 clearly shows the two layers (Fig. 8a). The fact that the vertical profile of CO does not show a clear separation, indicates that rather pristine air masses dominate both layers, which have not experienced strong pollution impact, but rather biogenic impact mainly affecting CO_2. If we additionally use this information, we can separate three distinct air masses. The region with lowest potential temperatures ($\Theta < 285$ K) has small (large) mixing ratios of CO (CO_2) and is mostly isolated from

15   mid-latitude influence. These air masses are most likely remnants of the spring time polar dome and we refer to this as the aged polar dome. Between 285 K and 299 K the air masses still show signatures of the polar dome while also the influence from mid-latitudes increases, indicated by lower CO_2 mixing ratios. This region is capped in the vertical by the polar dome boundary between 299 and 303.5 K. Above and thus outside the polar dome, mixing ratios of both species clearly show characteristics

Table 2. Maximum potential temperature and median latitude values for the polar dome boundary. Included are also the boundary values used for separating the different regions identified for further analysis.

	Maximum potential temperature	Median latitude
July 2014, polar dome boundary	299.0 - 303.5 K	73.5 °N
April 2015, polar dome boundary	283.5 and 287.5 K	66.0 °N - 68.5 °N
July 2014, aged polar dome	$\Theta_{max} < 285.0\,\mathrm{K}$	$Lat_{med} > 73.5\,°N$
July 2014, mixing region	$285.0\,\mathrm{K} < \Theta_{max} < 299.0\,\mathrm{K}$	$Lat_{med} > 73.5\,°N$
July 2014, outside polar dome	$\Theta_{max} > 303.5\,\mathrm{K}$	$Lat_{med} < 73.5\,°N$
April 2015, polar dome	$\Theta_{max} < 283.5\,\mathrm{K}$	$Lat_{med} > 68.5\,°N$
April 2015, outside polar dome	$\Theta_{max} > 287.5\,\mathrm{K}$	$Lat_{med} < 66.0\,°N$

of mid-latitude influence. Similar values to those observed outside the polar dome were also found in the mid-latitude lower troposphere for example at the Mace Head observatory in Ireland (see Fig. 4). A summary of the values for the polar dome boundary and the boundaries of the three different regions for July 2014 can be found in Tab. 2.

The threefold structure of the high Arctic lower troposphere, based on the derived boundary values for each region summa-
5 rized in Tab. 2, is further evident in the CO-CO_2 tracer-tracer correlation in Fig. 9a. More precisely, the aged polar dome (blue dots) seems to be a subset of the mixing region (green dots) indicated by a narrow group of data points at end of the highest CO_2 and lowest CO mixing ratios. The aged polar dome region is furthermore clearly separated from the region outside (red dots). The green dots indicate the influence of mixing between dome air and extra-dome air and correspond to the mixing region in the high Arctic between 285 and 299 K (compare Fig. 7b).

10 The tracer derived polar dome boundary for the April 2015 measurements was on average determined between 66.0 °N and 68.5 °N (blue bar in Fig. 8d; interquartile range: 65.0 °N - 69.5 °N) for the latitudinal value and between potential temperatures of 283.5 and 287.5 K (blue bar in Fig. 8c; interquartile range: 280.5 and 291.5 K). Values for the polar dome boundary are also summarized in Tab. 2 for April 2015. During spring the CO-CO_2 tracer-tracer correlation in Fig. 9b indicates at least three distinct branches. The separation of air masses between inside the polar dome and outside is based on the tracer derived
15 polar dome boundary (see Tab. 2). The red branch with the highest CO and CO_2 mixing ratios can be associated with pollution events observed during flights in Inuvik. In contrast, the red branch with highest CO_2 but relatively low CO values corresponds to observations in the unpolluted lower troposphere in the Inuvik region. Both branches are clearly associated with air masses outside the polar dome, since measurements around Inuvik were mostly performed outside the determined polar dome boundary. In contrast the blue branch represents the measurements inside the polar dome. These data points show different slopes
20 indicating different air mass properties. Within the polar dome region we observe a mixture of air masses which is evident from the relatively broad range of CO_2 and CO values forming a mixing line in Fig. 9b. The lowest CO and CO_2 values inside the polar dome (blue) can be associated with the lowest maximum potential temperatures and thus the highest residence time

within the dome area. Air masses with highest CO and CO_2 mixing ratios but still inside the polar dome (blue) originate at lower latitudes. In fact, ground stations in the potential source region two weeks before the time of the measurement campaign show enhanced CO and CO_2 values in the range of the upper branch of the scatter plot of those data points inside the polar dome. The observed mixture of air masses is also reported by Willis et al. (2019) who observed an altitude dependent com-

5 position and degree of processing of aerosol in the spring time polar dome. In their study, FLEXPART simulations suggest more southern source regions for those air masses with the highest potential temperatures within the polar dome. Furthermore, Schulz et al. (2019) determined an increase of refractive black carbon (rBC) and a decrease of the rBC mass-mean diameter with potential temperature inside the spring time polar dome, which was also associated to different source regions contributing to the observations.

10 ## 5.3 Transport regimes

In order to analyse the processes dominating the recent transport history of observed air masses, we apply the phase-space diagram introduced by Binder et al. (2017). In this analysis, we determine the maximum change in potential temperature ($\Delta\Theta$) as the difference between the potential temperature at the time of the measurement (Θ_0) and the previous potential temperature minimum or maximum (Θ_{min}, Θ_{max}) along the trajectory. Depending on which absolute difference is larger, the air mass has

15 either experienced diabatic heating ($\Delta\Theta = (\Theta_0 - \Theta_{min}) > 0$) or cooling ($\Delta\Theta = (\Theta_0 - \Theta_{max}) < 0$). An analogous analysis is made for the absolute temperature to determine if an air parcel predominantly gained or lost temperature before the measurement. This analysis allows us to cluster the data into four categories shown in Figs. 10a-d and 11a-c. The changes in potential temperature and temperature along the trajectories, indicated by the clusters, can be associated with processes affecting the respective air mass. Sector 1 ($\Delta\Theta < 0$, $\Delta T < 0$) mainly contains air masses that experienced diabatic cooling, which indicates

20 either thermal radiation, evaporation or low level transport over snow or ice covered regions (i.e. cold surfaces). In sector 2 ($\Delta\Theta > 0$, $\Delta T < 0$) air masses gained potential temperature, which indicates an ascending air mass that is diabatically heated by, for example, solar radiation or condensation processes. Sector 3 ($\Delta\Theta > 0$, $\Delta T > 0$) includes those air masses that experienced both an increase in temperature and potential temperature probably due to solar insolation. Finally, sector 4 ($\Delta\Theta < 0$, $\Delta T > 0$) combines air masses that lost potential temperature and gained temperature during transport. These air masses are diabatically

25 cooled and thus experienced a descent. We apply this clustering approach to identify differences between observations in the different regions (polar dome, outside polar dome, etc.) and to study whether we can connect trace gas mixing ratios to the dominant process in a specific region. The different regions were separated based on the tracer derived polar dome boundary (see Tab. 2) .

For July 2014, three regions are of particular interest, (1) the aged polar dome, (2) the mixing region and (3) the region

30 outside the polar dome (see Figs. 10a-d). Within the aged polar dome sector 3 dominates, thus solar insolation is important for heating the lowest levels. Air masses residing at the lowest altitude experienced diabatic heating potentially resulting in a slow and shallow convective lift of the air masses prior to the time of the measurement. Equal contributions come from sectors 1 and 4, dominated by diabatic cooling either through descent, low level transport over cold surfaces or evaporation. Almost none of the air masses are in sector 2, thus a significant ascent of air masses within the aged polar dome hardly occurs. In
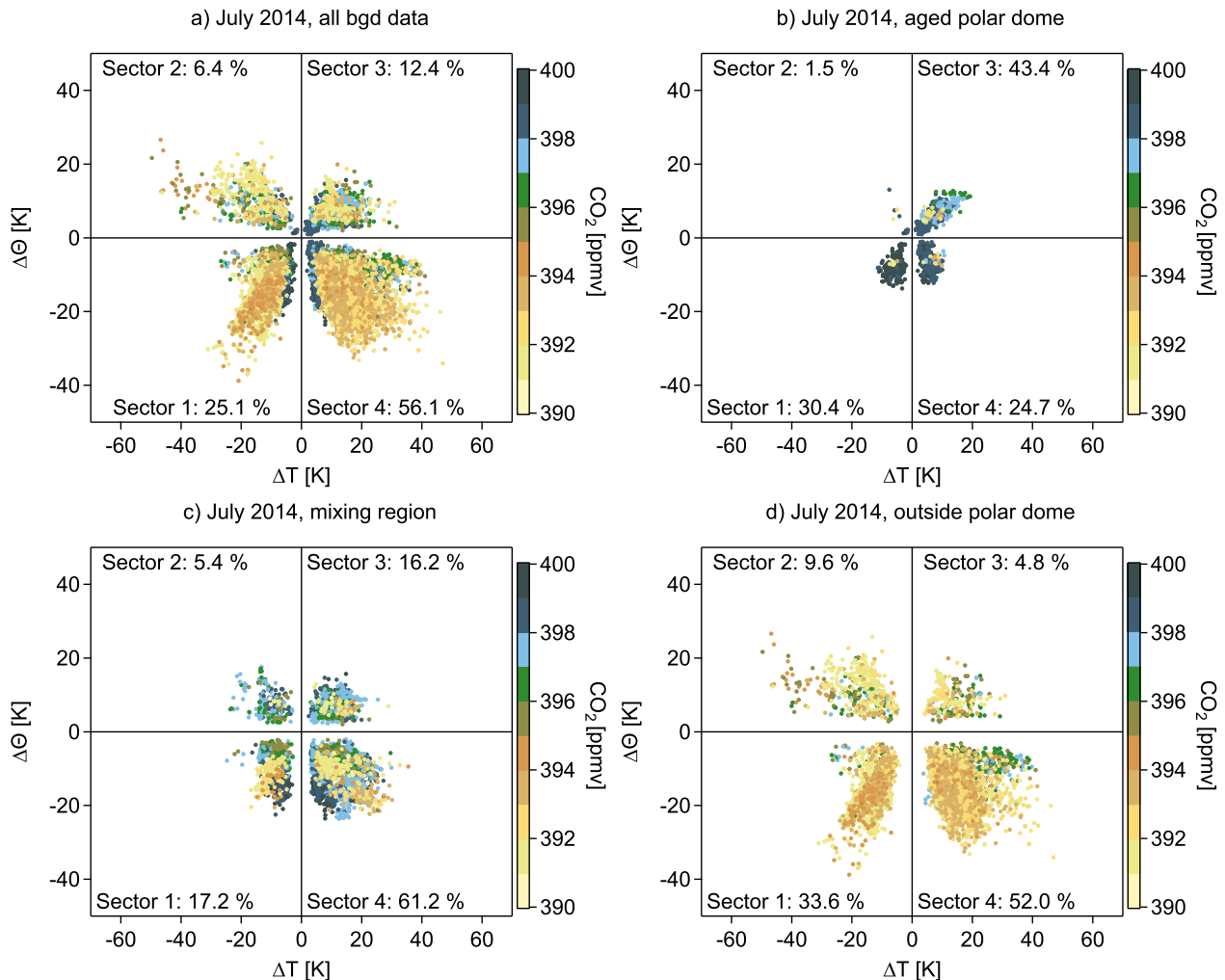
Figure 10. Phase-space diagram illustrating the maximum absolute change in temperature (ΔT) and potential temperature ($\Delta\Theta$) relative to the time of the measurement for July 2014. The colour code denotes the CO_2 mixing ratio at the time of the measurement. (a) shows all background data, (b) shows only those data corresponding to the aged polar dome. (c) shows the data points within the mixing region whereas (d) includes all data points outside the polar dome. To separate the different regions the tracer derived polar dome boundaries are used (see Tab. 2).

contrast, outside the polar dome area sector 4 dominates and generally diabatic cooling occurs (sector 1 and 4). Thus within the polar dome local near-surface diabatic processes seem to mostly affect the air masses; this effect is also evident in air mass composition. Observed CO_2 mixing ratios are highest in the aged polar dome associated with aged Arctic air and negligible mid-latitude influence. Outside the polar dome, air masses have been transported into the Arctic and descended due to radiative

5   cooling. Associated CO_2 mixing ratios of these air masses are significantly lower and can be attributed to more mid-latitude
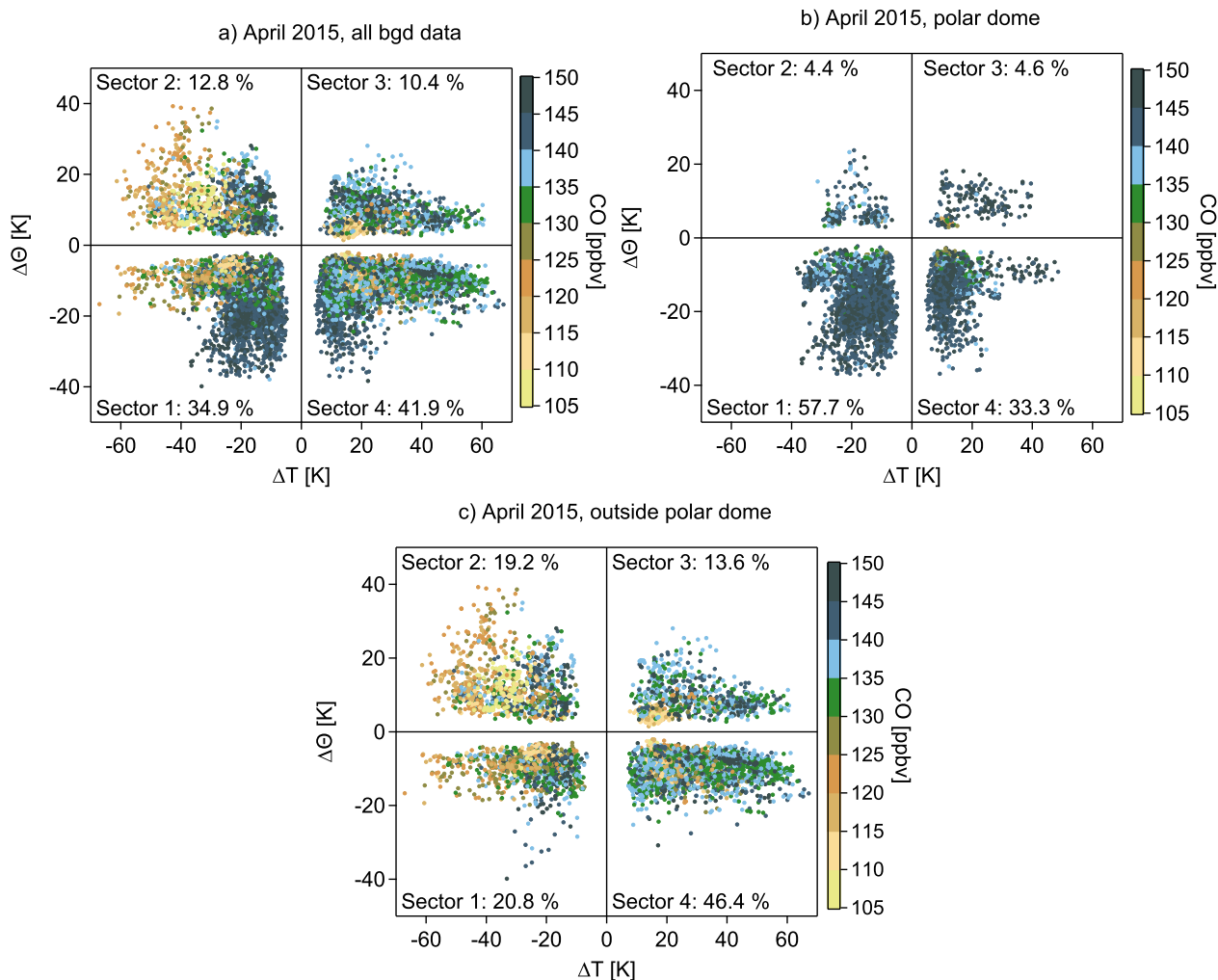
Figure 11. Phase-space diagram illustrating the maximum absolute change in temperature (ΔT) and potential temperature ($\Delta\Theta$) relative to the time of the measurement for April 2015. The colour code denotes the CO mixing ratio at the time of the measurement. (a) shows all background data, (b) only shows those data corresponding to the polar dome and (c) includes all data points outside the polar dome. To separate the different regions the tracer derived polar dome boundaries are used (see Tab. 2).

regions. Air masses associated with sector 4 experience descent once they have reached the high Arctic at higher altitudes. This can be regarded as a typical transport pathway during the summer with a fast uplift of air masses at mid-latitudes within convective and frontal systems followed by a northward movement and finally a descent into the high Arctic lower troposphere. Air masses in the mixing region are even more dominated by sector 4. Within this mixing region, trace gas concentrations still

5   show dome-like characteristics and low level processes seem to dominate over episodes of mid-latitude transport associated with air masses with lower CO_2 concentrations. Results for CO confirm the derived transport history for July 2014. A more
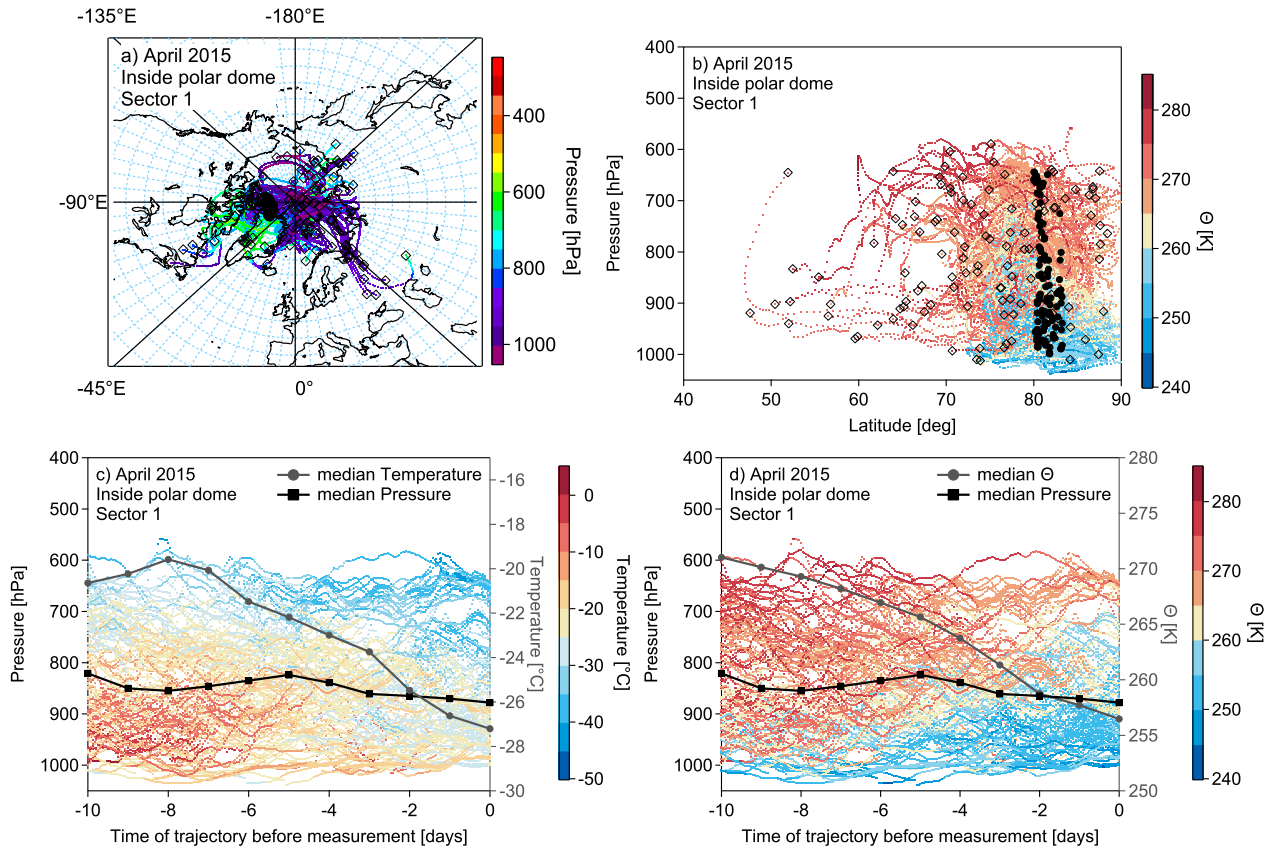
Figure 12. (a) Trajectories of the most dominant sector 1 for air masses inside the polar dome. The color code represents the pressure along the trajectories. (b) The same trajectories as in (a) as a function of pressure and latitude, color coded by potential temperature. In both figures (a) and (b) black circles denote the initialisation point of the trajectory along the flight track. The black open squares show the position of the trajectory 10 days back in time. Figures (c) and (d) show a vertical cross section of the trajectory evolution over the 10 days of travel with the color code denoting the temperature (c) and potential temperature (d). The black line marks the median pressure of the trajectory cluster at the individual time steps and the grey line indicates the median temperature and median potential temperature, respectively. Note that in all figures only every 20th trajectory is plotted for figure clarity.

detailed analysis of the physical processes along the air mass trajectories can be found in the supplement material (Figs. S3, S4 and S5) to this paper.

In April 2015 the picture is quite different (see Figs. 11a-c). Inside the polar dome diabatic cooling dominates, in particular sector 1. This is caused by diabatic descent due to radiative cooling in the absence of sunlight. In addition, low level transport over cold surfaces significantly contributes to transport into the high Arctic. Associated mixing ratios of CO show rather large values that can be explained by the accumulation of anthropogenic pollution from inner Arctic and high northern mid-latitude sources during the winter months. In the absence of sunlight chemical loss is reduced leading to an increase in the CO
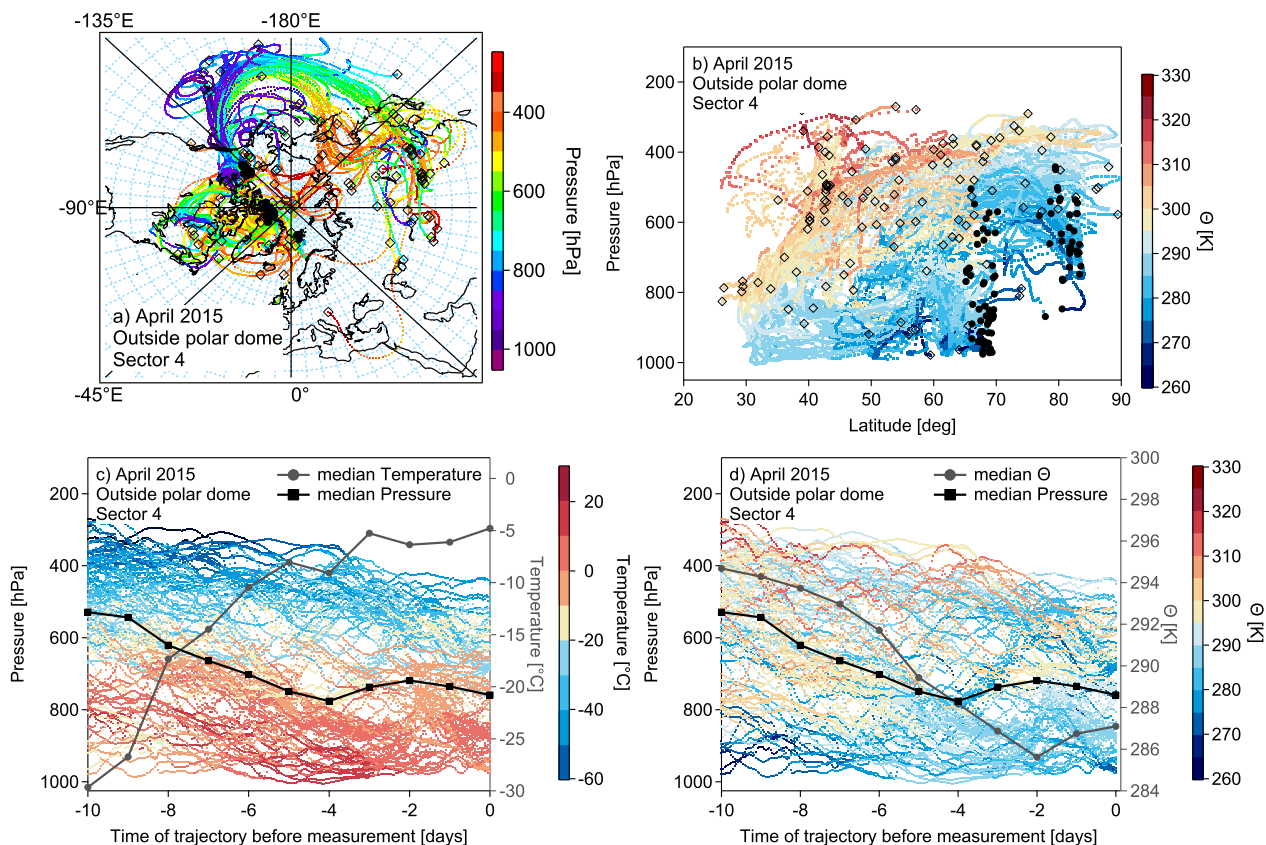
Figure 13. (a) Trajectories of the most dominant sector 4 for air masses outside the polar dome. The color code represents the pressure along the trajectories. (b) The same trajectories as in (a) as a function of pressure and latitude, color coded by potential temperature. In both figures (a) and (b) black circles denote the initialisation point of the trajectory along the flight track. The black open squares show the position of the trajectory 10 days back in time. Figures (c) and (d) show a vertical cross section of the trajectory evolution over the 10 days of travel with the color code denoting the temperature (c) and potential temperature (d). The black line marks the median pressure of the trajectory cluster at the individual time steps and the grey line indicates the median temperature and median potential temperature, respectively. Note that in all figures only every 20th trajectory is plotted for figure clarity.

atmospheric lifetime. Air masses within the polar dome are quite efficiently isolated from any significant southern mid-latitude influence. In contrast, outside the polar dome the picture is more diverse. Sector 4 dominates, thus diabatically cooled air masses potentially associated with the tendency to descent are observed. Input from various remote sources leads to stronger variations in CO mixing ratio. However, all sectors contribute with more than $10\,\%$ to the observed distribution. Our interpretation of air
5   mass transport history is confirmed by the results from CO_2.

Based on results from the phase space diagrams, we further analyzed the trajectories of the individual clusters. This allows for a more detailed analysis of the physical processes along the trajectory. We compare the two most dominant sectors for the

April 2015 measurements in Figs. 12a-d and 13a-d for air masses inside and outside the polar dome, respectively. Sector 1 is mostly dominated by air masses confined to the central Arctic at all altitude levels (see Figs. 12a and b). The air masses show a weak descent during the 10 day period before the measurements but experience a very pronounced decrease in temperature and potential temperature (see Figs. 12c and d, median trajectory cluster temperature). In contrast, air masses outside the polar dome, dominated by sector 4, contain contributions from different air streams. Air masses originate at different altitudes in the central Arctic, at low levels over the Pacific Ocean and from the upper troposphere over Asia. Air masses in this cluster are characterized by a significant increase in median temperature and decrease in median potential temperature indicating a descending trend, which is confirmed by decreasing median pressure over the time of travel. Low-level transport over the Pacific is associated with a low-pressure system over Alaska. Those air masses arrive at the polar dome boundary in the measurement region after experiencing a week net cooling over Alaska.

We conclude that air masses within the aged summertime polar dome are mostly confined to the boundary layer while they experienced a week diabatic warming due to insolation in July 2014 during NETCARE. In the mixing region and outside the polar dome diabatic cooling and a continuous descent is observed. Within the polar dome in April 2015 during NETCARE mostly near-surface processes (diabatic cooling due to the flow over cold surfaces) dominate the recent transport history of air masses in the lower polar dome. Air masses in the upper polar dome experience a very slow descent induced by radiative cooling. Outside the polar dome, air masses mostly arrive at higher potential temperatures in the Arctic and experience a continuous slow descent with increasing temperatures but only week diabatic cooling.

5.4 Chemical properties of the transport regimes

5.4.1 Trace gases

Using the tracer-derived polar dome boundary we compare the composition of air masses within the polar dome region and the surrounding region (Tab. 2). We make this comparison based on probability density functions (PDFs) of measured trace gases CO and CO_2 for July 2014 (see Figs. 14a and b) and April 2015 (see Figs. 14c and d).

For July 2014 the three different regions identified in Sec. 5.2 are confirmed by the respective PDFs for both species. The aged polar dome and the mixing region show a quite similar distribution for both species, except differences in the mode of the PDF, and are well separated from data outside the polar dome area. Whereas the absolute CO value inside the aged polar dome and the mixing region is lower compared to the area outside the polar dome, the CO_2 average mixing ratio within the polar dome is higher compared to the surrounding, as summarized in Tab. 3. This finding can be explained by the seasonal cycle of these two species and their zonal gradients (see data from NOAA ground based measurements in Fig. 4b). The minimum of the seasonal cycle of CO_2 in the Arctic and the mid-latitudes is reached at the end of the summer, typically during September. However, the onset of carbon uptake by vegetation in the mid-latitudes starts earlier compared to the high Arctic where less vegetation is present. At the same time the overall burden of CO_2 in the Arctic lower troposphere is to a large extent controlled by transport processes (Fung et al., 1983; Parazoo et al., 2011; Barnes et al., 2016). Mid-latitude air with relatively low CO_2 mixing ratios is transported to the high Arctic, in particular during the second phase of the campaign. But, as the polar dome
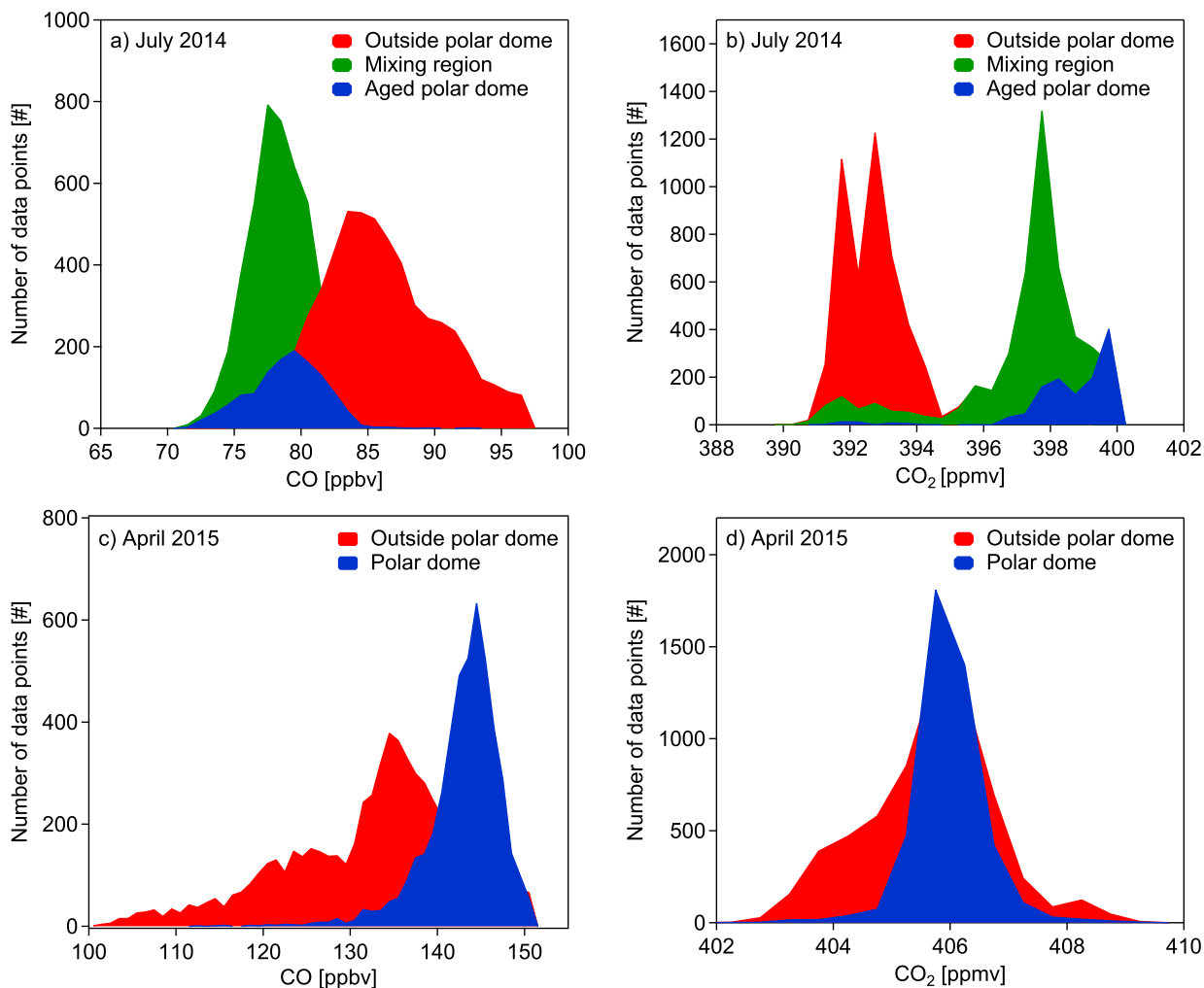
Figure 14. Probability density functions (PDFs) of all CO (a and c) and CO_2 (b and d) background measurements during July 2014 (upper panel) and April 2015 (lower panel). The median latitude and maximum potential temperature coordinates along the 10 day back trajectories were used for the separation between inside and outside the polar dome using the tracer derived polar dome boundaries (see Tab. 2).

acts as a transport barrier for those air masses, exchange of high Arctic lower tropospheric air with mid-latitude air is reduced leading to the observed PDF for CO_2. Under 24 h daylight conditions and with only a few inner Arctic sources of pollution, CO concentrations reach their minimum in the high Arctic in late summer. Air masses transported into the high Arctic from more southern regions are expected to have relatively high CO mixing ratios due to the seasonal cycle of CO that has a stronger amplitude in the Arctic compared to mid-latitudes (see Fig. 4a). Increased mid-latitude influence in the second half of the campaign enhanced the CO burden in the Arctic troposphere, whereas the inner Arctic air masses observed in the first half of the campaign were dominated by photochemically aged low CO air.

Table 3. Mean and median mixing ratios of CO and CO_2 inside and outside of the polar dome area using the tracer derived polar dome boundaries. The respective mixing ratios were calculated based on the minimum latitude and maximum potential temperature coordinates. Note that for the July 2014 dataset also the mixing ratios of the mixing region (MR) are included in the table.

	CO [ppbv]		CO_2 [ppmv]	
	inside polar dome	outside polar dome	inside polar dome	outside polar dome
	mean $\pm$ sdev (median)	mean $\pm$ sdev (median)	mean $\pm$ sdev (median)	mean $\pm$ sdev (median)
July 2014	78.8 ± 2.7 (79.1)	87.6 ± 7.2 (86.0)	398.6 ± 1.5 (399.0)	393.1 ± 1.6 (392.8)
July 2014, MR	78.8 ± 3.3 (78.5)		397.2 ± 2.0 (397.7)	
April 2015	142.9 ± 4.2 (143.6)	133.0 ± 9.9 (134.6)	406.0 ± 0.6 (405.9)	405.6 ± 1.1 (405.8)

We observed a strong link between trace gas distributions and the observed change in the synoptic situation from a more high pressure controlled regime to a synoptically active regime. Based on the trajectory simulations, increased mid-latitude influence was observed which in turn influenced the general concentration level of the trace gases CO and CO_2 (see supplement Fig. S6). CO increased from 77.9 ± 2.5 ppbv to 84.9 ± 4.7 ppbv. At the same time CO_2 decreased from 398.2 ± 1.0 ppmv to 393.8 ± 2.3 ppmv. Furthermore, increased variability in CO and CO_2 was observed, indicating enhanced entrainment of polluted mid-latitude air masses into the high Arctic. Part of the trajectories originating from outside the polar dome area pass the Northwestern Territories at low altitude, potentially within the boundary layer, where extensive biomass burning occured during the time of the measurements and before. Accordingly, increased aerosol concentrations during the second half of the campaign were reported by Burkart et al. (2017).

Using the polar dome boundary values listed in Tab. 2, Fig. 14 shows probability density functions for all CO (c) and CO_2 (d) background measurements during April 2015. Based on the PDFs, the difference in tropospheric trace gas composition within and outside the polar dome region is clearly visible for CO, but less distinct for CO_2. Average values for both species in the respective regions are also summarized in Tab. 3. In general, the distributions of CO and CO_2 are much narrower within the polar dome region and CO mixing ratios tend to be higher within the polar dome. For CO_2 the mean mixing ratio is quite similar within and outside the polar dome. However, a difference in the general distribution is observed. The reason for a less distinct separation between inside and outside the polar dome area is indicated by the seasonal cycles shown in Figs. 4a and b. CO_2 concentrations are on a plateau in spring, with reduced concentration changes with time and reduced latitudinal gradients. The CO mixing ratio has already started to decrease at the time of our measurements. However, the extent of the polar dome is much larger during the winter months and spring compared to the summer months. Hence more influence from northern mid-latitudes, and more mid-latitude pollution sources, are expected inside the dome area. CO rich air masses originate in cold regions of Eurasia and are able to reach the high Arctic lower troposphere where they are trapped during winter and early spring (Klonecki, 2003; Stohl, 2006; Jiao and Flanner, 2016). This leads to relatively large CO levels inside the polar dome compared to the region outside. In contrast, air masses from more southern mid-latitudes that are transported above the polar dome, have already experienced photochemical loss of CO near their source region.
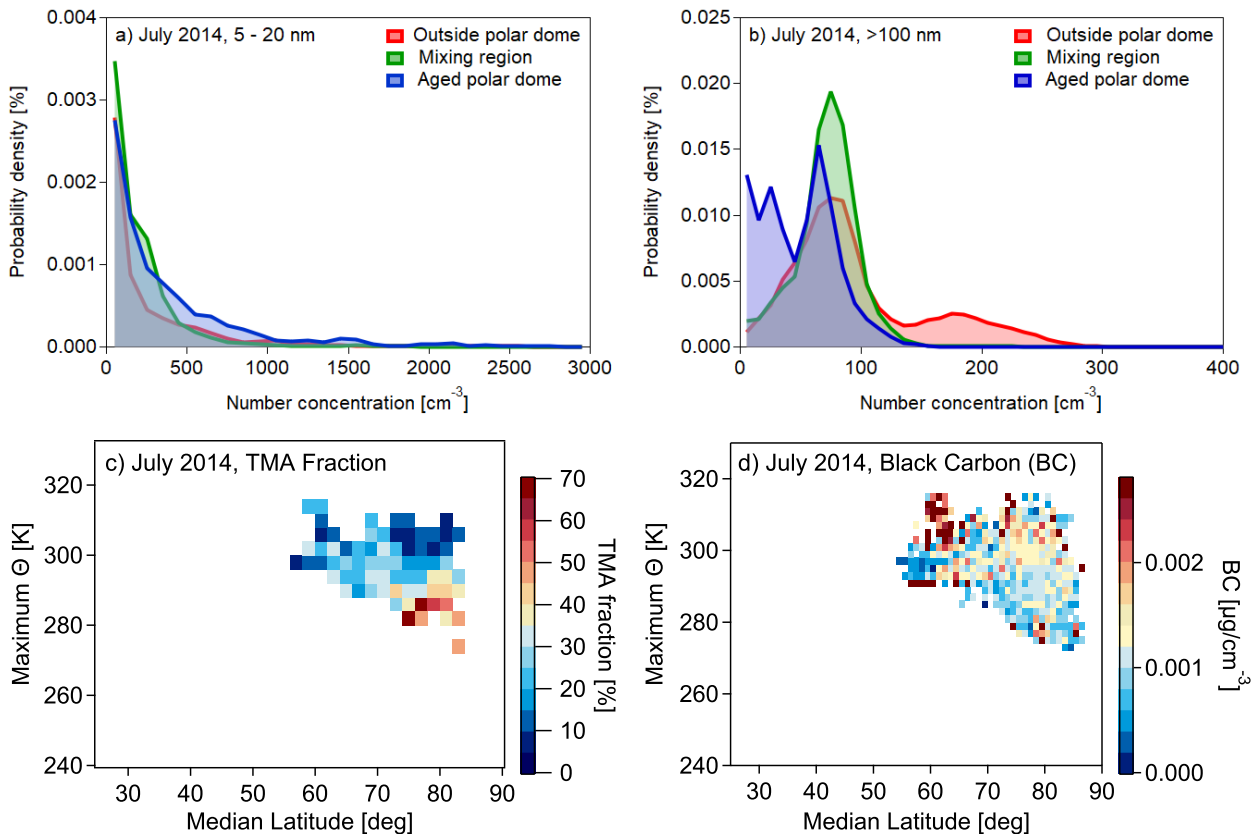
Figure 15. Normalized probability density functions for particles with diameters between 5 and 20 nm (a) and larger than 100 nm for July 2014 (b). The colour code represents the three different regions identified during the polar dome analysis. Panel (c) shows the distribution of the fraction of particles containing trimethylamine with respect to the total amount of particles measured by single particle mass spectrometry (Köllner et al., 2017) in the maximum potential temperature and median latitude coordinate system. Note that for the reason of particle spectra statistics the resolution of median latitude and maximum potential temperature interval is reduced compared to the refractory black carbon distribution (BC) shown in panel (d). The enhancement in BC within the polar dome is most probably due to fresh local pollution.

5.4.2 Aerosol

Having defined the polar dome based on trace gas gradients allows for a more detailed study on aerosol associated with the different air masses. Efficient wet removal and less efficient transport from lower latitudes lead to generally low aerosol concentrations (Stohl, 2006; Engvall et al., 2008) in the Arctic lower troposphere during summer. This is consistent with results in Fig. 15a and b. Observations of elevated levels of accumulation mode particles ($N_{>100}$) can be associated with regions outside the polar dome and subsequent transport to the measurement region. In parallel, regions within the polar dome were characterized by $N_{>100}$ smaller than $100\,\mathrm{cm}^{-3}$. In contrast, number concentrations of ultrafine particles (N_{5-20}) showed occasionally larger values within the polar dome compared to outside (Fig. 15a), indicating the formation of ultrafine

particles that occurred within the polar dome region (Burkart et al., 2017). Exemplary for aerosol composition, particulate trimethylamine (measured by single particle mass spectrometry) can be associated with sources within the polar dome (Fig. 15c), consistent with results in Köllner et al. (2017) and Willis et al. (2017). In contrast, the abundance of refractory black carbon can be linked to pollution sources outside the polar dome and subsequent transport to the measurement region (Fig. 15d) (Schulz et al., 2019). To conclude, the method introduced in this study is a useful tool to interpret Arctic aerosol observations in the context of transport processes and sources within and outside the polar dome region.

6 Discussion

Jiao and Flanner (2016) used the maximum zonal mean latitudinal gradient of $500\,\mathrm{hPa}$ geopotential height in the Northern Hemisphere to assess the impact of changes in atmospheric transport and removal processes due to climate change on the aerosol distribution in the Arctic. They deduced the polar dome boundary between 40 and $50\,°\mathrm{N}$ during January which is further south compared to our tracer derived values. However, their method does not account for the lower troposphere, which is essential for the diabatic processes affecting transport into the Arctic. For January, Klonecki (2003) determined a mixing barrier in the lower troposphere at $60\,°\mathrm{N}$ at longitudes between $60\,°\mathrm{W}$ and $105\,°\mathrm{W}$ for a short lived artificial tracer (7 days atmospheric lifetime) emitted in North America and Europe. During summer they reported that the strong mixing barrier moves north following the location of the Arctic front. This is in the range of our horizontal polar dome boundary for the respective spring (66.0 to $68.5\,°\mathrm{N}$) and summer ($73.5\,°\mathrm{N}$) season. In comparison to the location of the Arctic front, our analysis seems to give a more northern boundary for both July 2014 and April 2015. Furthermore, Klonecki (2003) reported an increasing mid-latitude influence with increasing altitude, in particular above $4\,\mathrm{km}$ altitude, which supports our findings of the potential temperature boundary being below $300\,\mathrm{K}$ for both seasons (corresponding to an altitude below $4\,\mathrm{km}$). Increasing mid-latitude influence with altitude is also in line with the results from Stohl (2006), who also used the Arctic front as a marker for the polar dome boundary.

The most isolated regions of the polar dome, where air masses experience the longest residence times, span a bigger area during late spring (April 2015) compared to summer (July 2014). This is in good agreement with previous studies, since it is already known that the polar dome extent is much smaller during summer compared to the winter months and processes and transport pathways controlling the composition of the high Arctic lower troposphere differ between both seasons (Klonecki, 2003; Stohl, 2006; Law and Stohl, 2007; Engvall et al., 2008; Garrett et al., 2010; Fuelberg et al., 2010). Our measurements during spring confirm a larger extent of the dome compared to summer and rather represent winter conditions than summer.

Stohl (2006) further defined an Arctic age of air and concluded that this age increased with decreasing altitude from 3 days between 5-8 km to around 1 week near the surface during the winter season (maximum 10 days in the North America region). During the summer season the air in the lowest $100\,\mathrm{m}$ of the troposphere is even older with values of 13-17 days north of $75\,°\mathrm{N}$. For a rough estimate of the upper limit of a transport timescale for mid-latitude air travelling into the summer polar dome during NETCARE, we can estimate the time at which the average mixing ratio within the polar dome was last observed at mid-latitude ground based observatories (for example Mace Head, Ireland). For CO_2, this suggests a transport time of

around three weeks, which is in the order of magnitude of the summertime Arctic age of air in the lowermost troposphere reported by Stohl (2006). This estimate assumes a transport controlled mixing ratio in the Arctic lower troposphere, which is justified by studies from Fung et al. (1983), Parazoo et al. (2011) and Barnes et al. (2016). Stohl (2006) further report that the Arctic troposphere is flushed on the time scales of 1-2 weeks in winter whereas in summer the corresponding timescale is twice as long. Assuming a similarly short Arctic age during the spring season this implies that above the polar dome air masses can be transported within days from mid-latitude regions to the Arctic troposphere. Tracer concentrations will be further homogenized along isentropic surfaces when diabatic processes are slow compared to transport timescales (Klonecki, 2003). This is evident in a layer of similar CO mixing ratios above the polar dome observed in April 2015 (see Fig. 7c). During July 2014, increased diabatic heating due to convective and boundary layer heating in mid-latitudes can lead to an uplift of air masses in mid-latitudes and further transport into the Arctic, which prevents an isentropic distribution during summer (Fig. 7a and b). Several studies analysed the transport of mid-latitude air masses into the Arctic troposphere above the polar dome along those pathways mentioned above, without explicit knowledge of the extent of the polar dome (Fuelberg et al., 2010; Roiger et al., 2011; Sodemann et al., 2011; Schmale et al., 2011; Brock et al., 2011; Ancellet et al., 2014, and references therein).

7   Summary and conclusion

In this study we defined the polar dome boundary based on tracer gradients. In July 2014, our results indicate that the horizontal polar dome boundary was located at a latitude of $73.5\,°$N. In the vertical a threefold structure established with the strongest trace gas gradient observed in a potential temperature range between 299 and 303.5 K, separating air masses within the polar dome from those outside. A second weaker gradient was found at a potential temperature of 285 K. We identified the region below 285 K as the aged polar dome, with the highest degree of isolation and thus the longest residence time of air masses. Between 285 K and 299 K a mixing region established. The mixing region shows significant characteristics of the polar dome region and clearly separates from outside the polar dome (see Fig. 9a). In April 2015 the tracer-derived polar dome boundary was between 66.0 and $68.5\,°$N and in a potential temperature range of 283.5 to 287.5 K.

The processes dominating recent (10 day) transport history were analyzed using a phase-space diagram based on Binder et al. (2017). For air masses outside the polar dome, diabatic cooling and a temperature increase was prevalent in both spring and summer (see Fig. 10d and Fig 11c). The associated transport pathway starts at mid-latitudes where air masses are lifted in convective or frontal systems followed by further northward motion towards the high Arctic, and finally descent into the lower Arctic troposphere. Previous studies have predominantly identified North America and Europe as the the major source region associated with this pathway (Klonecki, 2003; Stohl, 2006). These source regions are also indicated from our observations (Figs. S1 and S2); however, a more comprehensive study of the source regions is beyond the scope of this paper. Furthermore, air masses within the polar dome separate based on their transport history. During spring, air masses experience predominantly diabatic cooling and lose temperature which can be associated to low level transport over cold surfaces. During summer an efficient cooling mechanism is missing. In fact, already cold air masses within the polar dome potentially experience a weak heating thus leading to a conditionally unstable lower troposphere and potentially weak lifting. Diabatic cooling rates

determined from the trajectories are in good agreement with the range of 1 K per day (radiative cooling) to several degrees per day (contact with cold and mostly snow covered surface) reported for diabatic processes by Klonecki (2003).

Using our tracer derived polar dome boundaries, PDFs of CO and CO_2 concentrations inside and outside the polar dome clearly show a difference in the distribution and also in the absolute value of the distribution maximum. Tracer-tracer scatter plots indicate that the polar dome separates from the surrounding regions with a different slope (April 2015) or a narrow group of data points at the end of the highest CO_2 and lowest CO mixing ratios (July 2014). The PDFs and the scatter plots confirm different air mass properties inside and outside of the polar dome. For aerosol chemical composition, particles containing trimethylamine were enhanced inside the polar dome, indicating the influence of inner-Arctic sources whereas enhanced refractory black carbon concentrations outside the polar dome indicate remote sources of pollution.

We conclude that the differing chemical composition within and outside the polar dome allows for a trace gas gradient based definition of the polar dome boundary. Phase-space diagrams helped to cluster the air masses based on differing heating and cooling rates. This gives further insight in the processes that control recent transport history of the air masses within and outside the polar dome. The polar dome boundary derived in this study has already been used to study the source regions and chemical composition of aerosol within the polar dome (Schulz et al., 2019; Willis et al., 2019). Additionally, mixing and exchange processes along the polar dome boundary triggered by synoptic disturbances can be studied to shed light on additional pathways of mid-latitude pollution that reaches the Arctic lower troposphere. A polar dome boundary derived from gradients of chemical tracers can be further used for a quantification of the influence of inner Arctic and remote sources of pollution affecting the Arctic lower troposphere in a changing climate.

Data availability. All data from NETCARE are available on the Government of Canada Open Data Portal (https://open.canada.ca/data/en/dataset).

Author contributions. Author contributions. HB wrote the paper, with significant conceptual input from PH and DK and critical feedback from all co-authors. HB, FK, JS, MDW, JB, HS and WRL operated instruments in the field and analyzed resulting data. AAA analyzed flight data. WRL, JPDA and ABH designed the field experiment. DK ran LAGRANTO simulations, and HB analyzed the resulting data with input from DK.

Competing interests. The authors declare that they have no conflict of interest.

Acknowledgements. The authors acknowledge a large number of people for their contributions to this work. We thank Kenn Borek Air, in particular Kevin Elke, John Bayes, Gery Murtsel and Neil Travers, for their skillful piloting that facilitated these observations. We are grateful to John Ford, David Heath and the U of Toronto machine shop, Jim Hodgson and Lake Central Air Services in Muskoka, Jim Watson (Scale Modelbuilders, Inc.), Julia Binder and Martin Gehrmann (AWI), Mike Harwood and Andrew Elford (ECCC) for their support of the

integration of the instrumentation and aircraft. We thank Mohammed Wasey for his support of the instrumentation during the integration and in the field. We are grateful to Carrie Taylor (ECCC), Bob Christensen (U of T), Kevin Riehl (Kenn Borek Air), Lukas Kandora, Manuel Sellmann and Jens Herrmann (AWI), Desiree Toom, Sangeeta Sharma, Dan Veber, Andrew Platt, Anne Mari Macdonald, Ralf Staebler and Maurice Watt (ECCC), Kathy Law and Jennie Thomas (LATMOS) for their support of the study. We thank the biogeochemistry department

5   of MPIC for providing the CO instrument and Dieter Scharffe for his support during the preparation phase of the campaign. We thank the Nunavut Research Institute and the Nunavut Impact Review Board for licensing the study. Logistical support in Resolute Bay was provided by the Polar Continental Shelf Project (PCSP) of Natural Resources Canada under PCSP Field Project no. 218-14, and we are particularly grateful to Tim McCagherty and Jodi MacGregor of the PCSP. Funding for this work was provided by the Natural Sciences and Engineering Research Council of Canada through the NETCARE project of the Climate Change and Atmospheric Research Program, the Alfred Wegener

10   Institute and Environment and Climate Change Canada. All atmospheric data from Zeppelin are publicly available in the EBAS database (http: //ebas.nilu.no) and we thank Cathrine Lund Myhre and NILU - Norwegian Institute for Air Research for making the CO and CO_2 observations from Zeppelin available.

References

Abbatt, J. P. D., Leaitch, W. R., Aliabadi, A. A., Bertram, A. K., Blanchet, J.-P., Boivin-Rioux, A., Bozem, H., Burkart, J., Chang, R. Y. W., Charette, J., Chaubey, J. P., Christensen, R. J., Cirisan, A., Collins, D. B., Croft, B., Dionne, J., Evans, G. J., Fletcher, C. G., Galí, M., Ghahremaninezhad, R., Girard, E., Gong, W., Gosselin, M., Gourdal, M., Hanna, S. J., Hayashida, H., Herber, A. B., Hesaraki, S., Hoor, P., Huang, L., Hussherr, R., Irish, V. E., Keita, S. A., Kodros, J. K., Köllner, F., Kolonjari, F., Kunkel, D., Ladino, L. A., Law, K., Levasseur, M., Libois, Q., Liggio, J., Lizotte, M., Macdonald, K. M., Mahmood, R., Martin, R. V., Mason, R. H., Miller, L. A., Moravek, A., Mortenson, E., Mungall, E. L., Murphy, J. G., Namazi, M., Norman, A.-L., O'Neill, N. T., Pierce, J. R., Russell, L. M., Schneider, J., Schulz, H., Sharma, S., Si, M., Staebler, R. M., Steiner, N. S., Thomas, J. L., von Salzen, K., Wentzell, J. J. B., Willis, M. D., Wentworth, G. R., Xu, J.-W., and Yakobi-Hancock, J. D.: Overview paper: New insights into aerosol and climate in the Arctic, Atmos. Chem. Phys., 19, 2527–2560, https://doi.org/10.5194/acp-19-2527-2019, 2019.

Aliabadi, A. A., Thomas, J. L., Herber, A. B., Staebler, R. M., Leaitch, W. R., Schulz, H., Law, K. S., Marelle, L., Burkart, J., Willis, M. D., Bozem, H., Hoor, P. M., Köllner, F., Schneider, J., Levasseur, M., and Abbatt, J. P. D.: Ship emissions measurement in the Arctic by plume intercepts of the Canadian Coast Guard icebreaker Amundsen from the Polar 6 aircraft platform, Atmos. Chem. Phys., 16, 7899–7916, https://doi.org/10.5194/acp-16-7899-2016, 2016.

AMAP: AMAP assessment 2015: Black carbon and ozone as Arctic climate forcers, 2015.

Ancellet, G., Pelon, J., Blanchard, Y., Quennehen, B., Bazureau, A., Law, K. S., and Schwarzenboeck, A.: Transport of aerosol to the Arctic: analysis of CALIOP and French aircraft data during the spring 2008 POLARCAT campaign, Atmos. Chem. Phys., 14, 8235–8254, https://doi.org/10.5194/acp-14-8235-2014, 2014.

Arnold, S., Law, K., Brock, C., Thomas, J., Starkweather, S., von Salzen, K., Stohl, A., Sharma, S., Lund, M., Flanner, M., Petäjä, T., Tanimoto, H., Gamble, J., Dibb, J., Melamed, M., Johnson, N., Fidel, M., Tynkkynen, V.-P., Baklanov, A., Eckhardt, S., Monks, S., Browse, J., and Bozem, H.: Arctic air pollution: Challenges and opportunities for the next decade, Elem. Sci. Anth., 4, 000 104, https://doi.org/10.12952/journal.elementa.000104, 2016.

Barnes, E. A., Parazoo, N., Orbe, C., and Denning, A. S.: Isentropic transport and the seasonal cycle amplitude of CO_2, J. Geophys. Res. Atmos., pp. 8106–8124, https://doi.org/10.1002/2016JD025109, 2016.

Barrie, L. A.: Arctic air pollution: An overview of current knowledge, Atmos. Environ., 20, 643 – 663, https://doi.org/https://doi.org/10.1016/0004-6981(86)90180-0, first International Conference on Atmospheric Sciences and Applications to Air Quality, 1986.

Binder, H., Boettcher, M., Grams, C. M., Joos, H., Pfahl, S., and Wernli, H.: Exceptional Air Mass Transport and Dynamical Drivers of an Extreme Wintertime Arctic Warm Event, Geophys. Res. Lett., 44, 12,028–12,036, https://doi.org/10.1002/2017GL075841, 2017.

Bradley, R. S., Keimig, F. T., and Diaz, H. F.: Climatology of surface-based inversions in the North American Arctic, J. Geophys. Res., 97, 15 699, https://doi.org/10.1029/92JD01451, 1992.

Brock, C. A., Radke, L. F., and Hobbs, P. V.: Sulfur in particles in Arctic hazes derived from airborne in situ and lidar measurements, J. Geophys. Res., 95, 22 369, https://doi.org/10.1029/JD095iD13p22369, 1990.

Brock, C. A., Cozic, J., Bahreini, R., Froyd, K. D., Middlebrook, A. M., McComiskey, A., Brioude, J., Cooper, O. R., Stohl, A., Aikin, K. C., de Gouw, J. A., Fahey, D. W., Ferrare, R. A., Gao, R.-S., Gore, W., Holloway, J. S., Hübler, G., Jefferson, A., Lack, D. A., Lance, S., Moore, R. H., Murphy, D. M., Nenes, A., Novelli, P. C., Nowak, J. B., Ogren, J. A., Peischl, J., Pierce, R. B., Pilewskie, P., Quinn, P. K., Ryerson, T. B., Schmidt, K. S., Schwarz, J. P., Sodemann, H., Spackman, J. R., Stark, H., Thomson, D. S., Thornberry,

T., Veres, P., Watts, L. A., Warneke, C., and Wollny, A. G.: Characteristics, sources, and transport of aerosols measured in spring 2008 during the aerosol, radiation, and cloud processes affecting Arctic Climate (ARCPAC) Project, Atmos. Chem. Phys., 11, 2423–2453, https://doi.org/10.5194/acp-11-2423-2011, 2011.

Browse, J., Carslaw, K. S., Arnold, S. R., Pringle, K., and Boucher, O.: The scavenging processes controlling the seasonal cycle in Arctic sulphate and black carbon aerosol, Atmos. Chem. Phys., 12, 6775–6798, https://doi.org/10.5194/acp-12-6775-2012, 2012.

Burkart, J., Willis, M. D., Bozem, H., Thomas, J. L., Law, K., Hoor, P., Aliabadi, A. A., Köllner, F., Schneider, J., Herber, A., Abbatt, J. P. D., and Leaitch, W. R.: Summertime observations of elevated levels of ultrafine particles in the high Arctic marine boundary layer, Atmos. Chem. Phys., 17, 5515–5535, https://doi.org/10.5194/acp-17-5515-2017, 2017.

Carlson, T. N.: Speculations on the Movement of Polluted Air to the Arctic, Atmos. Environ., 15, 1473–1477, 1981.

Cohen, J., Screen, J. A., Furtado, J. C., Barlow, M., Whittleston, D., Coumou, D., Francis, J., Dethloff, K., Entekhabi, D., Overland, J., and Jones, J.: Recent Arctic amplification and extreme mid-latitude weather, Nat. Geosci., 7, 627–637, https://doi.org/10.1038/ngeo2234, 2014.

Corbett, J. J., Lack, D. A., Winebrake, J. J., Harder, S., Silberman, J. a., and Gold, M.: Arctic shipping emissions inventories and future scenarios, Atmos. Chem. Phys., 10, 9689–9704, https://doi.org/10.5194/acp-10-9689-2010, 2010.

Crawford, A. and Serreze, M.: A New Look at the Summer Arctic Frontal Zone, J. Clim., 28, 737–754, https://doi.org/10.1175/JCLI-D-14-00447.1, 2015.

Dianov-Klokov, V. I. and Yurganov, L. N.: Spectroscopic measurements of atmospheric carbon monoxide and methane. 2: Seasonal variations and long-term trends, J. Atmos. Chem., 8, 153–164, https://doi.org/10.1007/BF00053720, 1989.

Dlugokencky, E., Lang, P., Mund, J., Crotwell, A., Crotwell, M., and Thoning, K.: Atmospheric Carbon Dioxide Dry Air Mole Fractions from the NOAA ESRL Carbon Cycle Cooperative Global Air Sampling Network, Version: 2017-10-17, 1968–2017, ftp://aftp.cmdl.noaa.gov/data/trace_gases/co2/flask/surface/., 2018.

Dreiling, V. and Friederich, B.: Spatial distribution of the arctic haze aerosol size distribution in western and eastern Arctic, Atmos. Res., 44, 133–152, https://doi.org/10.1016/S0169-8095(96)00035-X, 1997.

Eckhardt, S., Hermansen, O., Grythe, H., Fiebig, M., Stebel, K., Cassiani, M., Baecklund, A., and Stohl, A.: The influence of cruise ship emissions on air pollution in Svalbard - a harbinger of a more polluted Arctic?, Atmos. Chem. Phys., 13, 8401–8409, https://doi.org/10.5194/acp-13-8401-2013, 2013.

Engvall, A.-C., Krejci, R., Ström, J., Treffeisen, R., Scheele, R., Hermansen, O., and Paatero, J.: Changes in aerosol properties during spring-summer period in the Arctic troposphere, Atmos. Chem. Phys., 8, 445–462, https://doi.org/10.5194/acp-8-445-2008, 2008.

Fisher, J. A., Jacob, D. J., Purdy, M. T., Kopacz, M., Le Sager, P., Carouge, C., Holmes, C. D., Yantosca, R. M., Batchelor, R. L., Strong, K., Diskin, G. S., Fuelberg, H. E., Holloway, J. S., Hyer, E. J., McMillan, W. W., Warner, J., Streets, D. G., Zhang, Q., Wang, Y., and Wu, S.: Source attribution and interannual variability of Arctic pollution in spring constrained by aircraft (ARCTAS, ARCPAC) and satellite (AIRS) observations of carbon monoxide, Atmos. Chem. Phys., 10, 977–996, https://doi.org/10.5194/acp-10-977-2010, 2010.

Flanner, M. G., Zender, C. S., Randerson, J. T., and Rasch, P. J.: Present-day climate forcing and response from black carbon in snow, J. Geophys. Res., 112, D11 202, https://doi.org/10.1029/2006JD008003, 2007.

Forkel, M., Carvalhais, N., Rodenbeck, C., Keeling, R., Heimann, M., Thonicke, K., Zaehle, S., and Reichstein, M.: Enhanced seasonal CO_2 exchange caused by amplified plant productivity in northern ecosystems, Science, 351, 696–699, https://doi.org/10.1126/science.aac4971, 2016.

Francis, J. A. and Vavrus, S. J.: Evidence linking Arctic amplification to extreme weather in mid-latitudes, Geophys. Res. Lett., 39, n/a–n/a, https://doi.org/10.1029/2012GL051000, 2012.

Francis, J. A., Vavrus, S. J., and Cohen, J.: Amplified Arctic warming and mid-latitude weather: new perspectives on emerging connections, Wiley Interdiscip. Rev. Clim. Chang., 8, e474, https://doi.org/10.1002/wcc.474, 2017.

5 Fuelberg, H. E., Harrigan, D. L., and Sessions, W.: A meteorological overview of the ARCTAS 2008 mission, Atmos. Chem. Phys., 10, 817–842, https://doi.org/10.5194/acp-10-817-2010, 2010.

Fung, I., Prentice, K., Matthews, E., Lerner, J., and Russell, G.: Three-dimensional tracer model study of atmospheric CO_2: Response to seasonal exchanges with the terrestrial biosphere, J. Geophys. Res., 88, 1281, https://doi.org/10.1029/JC088iC02p01281, 1983.

Garrett, T. J., Zhao, C., and Novelli, P. C.: Assessing the relative contributions of transport efficiency and scavenging to seasonal variability

10 in Arctic aerosol, Tellus, Ser. B Chem. Phys. Meteorol., 62, 190–196, https://doi.org/10.1111/j.1600-0889.2010.00453.x, 2010.

Gerbig, C., Schmitgen, S., Kley, D., Volz-Thomas, A., Dewey, K., and Haaks, D.: An improved fast-response vacuum-UV resonance fluorescence CO instrument, J. Geophys. Res. Atmos., 104, 1699–1704, https://doi.org/10.1029/1998JD100031, 1999.

Hall, A.: The Role of Surface Albedo Feedback in Climate, J. Clim., 17, 1550–1568, https://doi.org/10.1175/1520-0442(2004)017<1550:TROSAF>2.0.CO;2, 2004.

15 Hansen, J. and Nazarenko, L.: Trends of measured climate forcing agents, PNAS, 98, 14 778–14 783, https://doi.org/10.1073/pnas.261553698, 2004.

Hecobian, A., Liu, Z., Hennigan, C. J., Huey, L. G., Jimenez, J. L., Cubison, M. J., Vay, S., Diskin, G. S., Sachse, G. W., Wisthaler, A., Mikoviny, T., Weinheimer, A. J., Liao, J., Knapp, D. J., Wennberg, P. O., Kürten, A., Crounse, J. D., Clair, J. S., Wang, Y., and Weber, R. J.: Comparison of chemical characteristics of 495 biomass burning plumes intercepted by the NASA DC-8 aircraft during the

20 ARCTAS/CARB-2008 field campaign, Atmos. Chem. Phys., 11, 13 325–13 337, https://doi.org/10.5194/acp-11-13325-2011, 2011.

Herber, A., Dethloff, K., Haas, C., Steinhage, D., Strapp, J. W., Bottenheim, J., McElroy, T., and Yamanouchi, T.: POLAR 5 - a new research aircraft for improved access to the Arctic, in: ISAR-1, Drastic Chang. under Glob. Warm. Ext. Abstr., pp. 54–57, 2008.

Hirdman, D., Sodemann, H., Eckhardt, S., Burkhart, J. F., Jefferson, A., Mefford, T., Quinn, P. K., Sharma, S., Ström, J., and Stohl, A.: Source identification of short-lived air pollutants in the Arctic using statistical analysis of measurement data and particle dispersion model

25 output, Atmos. Chem. Phys., 10, 669–693, https://doi.org/10.5194/acp-10-669-2010, 2010.

Holland, M. M. and Bitz, C. M.: Polar amplification of climate change in coupled models, Clim. Dyn., 21, 221–232, https://doi.org/10.1007/s00382-003-0332-6, 2003.

Holloway, T., Ii, H. L., and Kasibhatla, P. S.: Global distribution of carbon monoxide, J. Geophys. Res., 105, 2000.

IPCC: Technical Summary, book section TS, p. 33–115, Cambridge University Press, Cambridge, United Kingdom and New York, NY, USA,

30 https://doi.org/10.1017/CBO9781107415324.005, 2013.

Iversen, T.: On the atmospheric transport of pollution to the Arctic, Geophys. Res. Lett., 11, 457–460, https://doi.org/10.1029/GL011i005p00457, 1984.

Jeffries, M. O., Overland, J. E., and Perovich, D. K.: The Arctic shifts to a new normal, Phys. Today, 66, 35–40, https://doi.org/10.1063/PT.3.2147, 2013.

35 Jiao, C. and Flanner, M. G.: Changing black carbon transport to the Arctic from present day to the end of 21st century, J. Geophys. Res. Atmos., 121, 4734–4750, https://doi.org/10.1002/2015JD023964, 2016.

Keeling, C. D., Chin, J. F. S., and Whorf, T. P.: Increased activity of northern vegetation inferred from atmospheric CO_2 measurements, Nature, 382, 146–149, https://doi.org/10.1038/382146a0, 1996.

Klonecki, A.: Seasonal changes in the transport of pollutants into the Arctic troposphere-model study, J. Geophys. Res., 108, 8367, https://doi.org/10.1029/2002JD002199, 2003.

Koch, D. and Hansen, J.: Distant origins of Arctic black carbon: A Goddard Institute for Space Studies ModelE experiment, J. Geophys. Res., 110, D04 204, https://doi.org/10.1029/2004JD005296, 2005.

5 Köllner, F., Schneider, J., Willis, M. D., Klimach, T., Helleis, F., Bozem, H., Kunkel, D., Hoor, P., Burkart, J., Leaitch, W. R., Aliabadi, A. A., Abbatt, J. P. D., Herber, A. B., and Borrmann, S.: Particulate trimethylamine in the summertime Canadian high Arctic lower troposphere, Atmos. Chem. Phys., 17, 13 747–13 766, https://doi.org/10.5194/acp-17-13747-2017, 2017.

Law, K. S. and Stohl, A.: Arctic Air Pollution: Origins and Impacts, Science, 315, 1537–1540, https://doi.org/10.1126/science.1137695, 2007.

10 Law, K. S., Stohl, A., Quinn, P. K., Brock, C. A., Burkhart, J. F., Paris, J.-D., Ancellet, G., Singh, H. B., Roiger, A., Schlager, H., Dibb, J., Jacob, D. J., Arnold, S. R., Pelon, J., and Thomas, J. L.: Arctic Air Pollution: New Insights from POLARCAT-IPY, Bull. Am. Meteorol. Soc., 95, 1873–1895, https://doi.org/10.1175/BAMS-D-13-00017.1, 2014.

Leaitch, W. R., Korolev, A., Aliabadi, A. A., Burkart, J., Willis, M. D., Abbatt, J. P. D., Bozem, H., Hoor, P., Köllner, F., Schneider, J., Herber, A., Konrad, C., and Brauner, R.: Effects of 20–100 nm particles on liquid clouds in the clean summertime Arctic, Atmos. Chem. Phys.,
15 16, 11 107–11 124, https://doi.org/10.5194/acp-16-11107-2016, 2016.

Lee, M.-Y., Hong, C.-C., and Hsu, H.-H.: Compounding effects of warm sea surface temperature and reduced sea ice on the extreme circulation over the extratropical North Pacific and North America during the 2013-2014 boreal winter, Geophys. Res. Lett., 42, 1612–1618, https://doi.org/10.1002/2014GL062956, 2015.

Libois, Q., Ivanescu, L., Blanchet, J.-P., Schulz, H., Bozem, H., Leaitch, W. R., Burkart, J., Abbatt, J. P. D., Herber, A. B., Aliabadi,
20 A. A., and Girard, É.: Airborne observations of far-infrared upwelling radiance in the Arctic, Atmos. Chem. Phys., 16, 15 689–15 707, https://doi.org/10.5194/acp-16-15689-2016, 2016.

Lindsay, R. and Schweiger, A.: Arctic sea ice thickness loss determined using subsurface, aircraft, and satellite observations, Cryosphere, 9, 269–283, https://doi.org/10.5194/tc-9-269-2015, 2015.

McConnell, J. R., Edwards, R., Kok, G. L., Flanner, M. G., Zender, C. S., Saltzman, E. S., Banta, J. R., Pasteris, D. R., Carter,
25 M. M., and Kahl, J. D. W.: 20th-century industrial black carbon emissions altered Arctic climate forcing., Science, 317, 1381–4, https://doi.org/10.1126/science.1144856, 2007.

Melia, N., Haines, K., and Hawkins, E.: Sea ice decline and 21st century trans-Arctic shipping routes, Geophys. Res. Lett., 43, 9720–9728, https://doi.org/10.1002/2016GL069315, 2016.

Monks, S. a., Arnold, S. R., Emmons, L. K., Law, K. S., Turquety, S., Duncan, B. N., Flemming, J., Huijnen, V., Tilmes, S., Langner, J.,
30 Mao, J., Long, Y., Thomas, J. L., Steenrod, S. D., Raut, J. C., Wilson, C., Chipperfield, M. P., Diskin, G. S., Weinheimer, A., Schlager, H., and Ancellet, G.: Multi-model study of chemical and physical controls on transport of anthropogenic and biomass burning pollution to the Arctic, Atmos. Chem. Phys., 15, 3575–3603, https://doi.org/10.5194/acp-15-3575-2015, 2015.

Novelli, P. C., Masarie, K. A., and Lang, P. M.: Distributions and recent changes of carbon monoxide in the lower troposphere, J. Geophys. Res. Atmos., 103, 19 015–19 033, https://doi.org/10.1029/98JD01366, 1998.

35 Parazoo, N. C., Denning, A. S., Berry, J. A., Wolf, A., Randall, D. A., Kawa, S. R., Pauluis, O., and Doney, S. C.: Moist synoptic transport of CO_2 along the mid-latitude storm track, Geophys. Res. Lett., 38, n/a–n/a, https://doi.org/10.1029/2011GL047238, 2011.

Peters, G. P., Nilssen, T. B., Lindholt, L., Eide, M. S., Glomsrød, S., Eide, L. I., and Fuglestvedt, J. S.: Future emissions from shipping and petroleum activities in the Arctic, Atmos. Chem. Phys., 11, 5305–5320, https://doi.org/10.5194/acp-11-5305-2011, 2011.

Petron, G., Crotwell, A., Lang, P., and Dlugokencky, E.: Atmospheric Carbon Monoxide Dry Air Mole Fractions from the NOAA ESRL Carbon Cycle Cooperative Global Air Sampling Network, Version: 2018-07-31, 1988–2017, ftp://aftp.cmdl.noaa.gov/data/trace_gases/co/flask/surface/, 2018.

Pithan, F. and Mauritsen, T.: Arctic amplification dominated by temperature feedbacks in contemporary climate models, Nat. Geosci., 7, 181–184, https://doi.org/10.1038/ngeo2071, 2014.

Pithan, F., Svensson, G., Caballero, R., Chechin, D., Cronin, T. W., Ekman, A. M. L., Neggers, R., Shupe, M. D., Solomon, A., Tjernström, M., and Wendisch, M.: Role of air-mass transformations in exchange between the Arctic and mid-latitudes, Nat. Geosci., 11, 805–812, https://doi.org/10.1038/s41561-018-0234-1, 2018.

Quinn, P. K., Bates, T. S., Baum, E., Doubleday, N., Fiore, A. M., Flanner, M., Fridlind, A., Garrett, T. J., Koch, D., Menon, S., Shindell, D., Stohl, A., and Warren, S. G.: Short-lived pollutants in the Arctic: their climate impact and possible mitigation strategies, Atmos. Chem. Phys., 8, 1723–1735, https://doi.org/10.5194/acp-8-1723-2008, 2008.

Raatz, W. E.: Meteorological conditions over Eurasia and the Arctic contributing to the March 1983 Arctic haze episode, Geophys. Res. Lett., 19, 2121–2126, 1985.

Rahn, K. A.: Relative importances of North America and Eurasia as sources of arctic aerosol, Atmos. Environ., 15, 1447–1455, https://doi.org/10.1016/0004-6981(81)90351-6, 1981.

Robock, A.: Ice and Snow Feedbacks and the Latitudinal and Seasonal Distribution of Climate Sensitivity, J. Atmos. Sci., 40, 986–997, 1983.

Roiger, A., Schlager, H., Schäfler, A., Huntrieser, H., Scheibe, M., Aufmhoff, H., Cooper, O. R., Sodemann, H., Stohl, A., Burkhart, J., Lazzara, M., Schiller, C., Law, K. S., and Arnold, F.: In-situ observation of Asian pollution transported into the Arctic lowermost stratosphere, Atmos. Chem. Phys., 11, 10 975–10 994, https://doi.org/10.5194/acp-11-10975-2011, 2011.

Scharffe, D., Slemr, F., Brenninkmeijer, C. A. M., and Zahn, A.: Carbon monoxide measurements onboard the CARIBIC passenger aircraft using UV resonance fluorescence, Atmos. Meas. Tech., 5, 1753–1760, https://doi.org/10.5194/amt-5-1753-2012, 2012.

Schmale, J., Schneider, J., Ancellet, G., Quennehen, B., Stohl, A., Sodemann, H., Burkhart, J. F., Hamburger, T., Arnold, S. R., Schwarzenboeck, A., Borrmann, S., and Law, K. S.: Source identification and airborne chemical characterisation of aerosol pollution from long-range transport over Greenland during POLARCAT summer campaign 2008, Atmos. Chem. Phys., 11, 10 097–10 123, https://doi.org/10.5194/acp-11-10097-2011, 2011.

Schmale, J., Arnold, S. R., Law, K. S., Thorp, T., Anenberg, S., Simpson, W. R., Mao, J., and Pratt, K. A.: Local Arctic Air Pollution: A Neglected but Serious Problem, Earth's Futur., 6, 1385–1412, https://doi.org/10.1029/2018EF000952, 2018.

Schulz, H., Zanatta, M., Bozem, H., Leaitch, W. R., Herber, A. B., Burkart, J., Willis, M. D., Kunkel, D., Hoor, P. M., Abbatt, J. P. D., and Gerdes, R.: High Arctic aircraft measurements characterising black carbon vertical variability in spring and summer, Atmos. Chem. Phys., 19, 2361–2384, https://doi.org/10.5194/acp-19-2361-2019, 2019.

Screen, J. A. and Simmonds, I.: The central role of diminishing sea ice in recent Arctic temperature amplification, Nature, 464, 1334–1337, https://doi.org/10.1038/nature09051, 2010.

Serreze, M. C., Lynch, A. H., and Clark, M. P.: The Arctic Frontal Zone as Seen in the NCEP–NCAR Reanalysis, J. Clim., 14, 1550–1567, https://doi.org/10.1175/1520-0442(2001)014<1550:TAFZAS>2.0.CO;2, 2001.

Sharma, S., Andrews, E., Barrie, L. A., Ogren, J. A., and Lavoué, D.: Variations and sources of the equivalent black carbon in the high Arctic revealed by long-term observations at Alert and Barrow: 1989–2003, J. Geophys. Res., 111, D14 208, https://doi.org/10.1029/2005JD006581, 2006.

Sharma, S., Ishizawa, M., Chan, D., Lavoué, D., Andrews, E., Eleftheriadis, K., and Maksyutov, S.: 16-year simulation of Arctic black carbon: Transport, source contribution, and sensitivity analysis on deposition, J. Geophys. Res. Atmos., 118, 943–964, https://doi.org/10.1029/2012JD017774, 2013.

Shindell, D. and Faluvegi, G.: Climate response to regional radiative forcing during the twentieth century, Nat. Geosci., 2, 294–300, https://doi.org/10.1038/ngeo473, 2009.

Shindell, D. T., Chin, M., Dentener, F., Doherty, R. M., Faluvegi, G., Fiore, A. M., Hess, P., Koch, D. M., MacKenzie, I. A., Sanderson, M. G., Schultz, M. G., Schulz, M., Stevenson, D. S., Teich, H., Textor, C., Wild, O., Bergmann, D. J., Bey, I., Bian, H., Cuvelier, C., Duncan, B. N., Folberth, G., Horowitz, L. W., Jonson, J., Kaminski, J. W., Marmer, E., Park, R., Pringle, K. J., Schroeder, S., Szopa, S., Takemura, T., Zeng, G., Keating, T. J., and Zuber, A.: A multi-model assessment of pollution transport to the Arctic, Atmos. Chem. Phys., 8, 5353–5372, https://doi.org/10.5194/acp-8-5353-2008, 2008.

Sodemann, H., Pommier, M., Arnold, S. R., Monks, S. a., Stebel, K., Burkhart, J. F., Hair, J. W., Diskin, G. S., Clerbaux, C., Coheur, P.-F., Hurtmans, D., Schlager, H., Blechschmidt, A.-M., Kristjánsson, J. E., and Stohl, A.: Episodes of cross-polar transport in the Arctic troposphere during July 2008 as seen from models, satellite, and aircraft observations, Atmos. Chem. Phys., 11, 3631–3651, https://doi.org/10.5194/acp-11-3631-2011, 2011.

Sprenger, M. and Wernli, H.: The LAGRANTO Lagrangian analysis tool – version 2.0, Geosci. Model Dev., 8, 2569–2586, https://doi.org/10.5194/gmd-8-2569-2015, 2015.

Stohl, A.: Characteristics of atmospheric transport into the Arctic troposphere, J. Geophys. Res., 111, D11 306, https://doi.org/10.1029/2005JD006888, 2006.

Stohl, A., Klimont, Z., Eckhardt, S., and Kupiainen, K.: Why models struggle to capture Arctic Haze: the underestimated role of gas flaring and domestic combustion emissions, Atmos. Chem. Phys. Discuss., 13, 9567–9613, https://doi.org/10.5194/acpd-13-9567-2013, 2013.

Stroeve, J. C., Kattsov, V., Barrett, A., Serreze, M., Pavlova, T., Holland, M., and Meier, W. N.: Trends in Arctic sea ice extent from CMIP5, CMIP3 and observations, Geophys. Res. Lett., 39, n/a–n/a, https://doi.org/10.1029/2012GL052676, 2012.

Wernli, H. and Davies, H. C.: A Lagrangian-based analysis of extratropical cyclones. I: The method and some applications, Q. J. R. Meteorol. Soc., 123, 467–489, https://doi.org/10.1256/smsqj.53810, 1997.

Willis, M. D., Burkart, J., Thomas, J. L., Köllner, F., Schneider, J., Bozem, H., Hoor, P. M., Aliabadi, A. A., Schulz, H., Herber, A. B., Leaitch, W. R., and Abbatt, J. P. D.: Growth of nucleation mode particles in the summertime Arctic: a case study, Atmos. Chem. Phys., 16, 7663–7679, https://doi.org/10.5194/acp-16-7663-2016, 2016.

Willis, M. D., Köllner, F., Burkart, J., Bozem, H., Thomas, J. L., Schneider, J., Aliabadi, A. A., Hoor, P. M., Schulz, H., Herber, A. B., Leaitch, W. R., and Abbatt, J. P.: Evidence for marine biogenic influence on summertime Arctic aerosol, Geophys. Res. Lett., 44, 6460–6470, https://doi.org/10.1002/2017GL073359, 2017.

Willis, M. D., Leaitch, W. R., and Abbatt, J. P.: Processes Controlling the Composition and Abundance of Arctic Aerosol, Rev. Geophys., 56, 621–671, https://doi.org/10.1029/2018RG000602, 2018.

Willis, M. D., Bozem, H., Kunkel, D., Lee, A. K. Y., Schulz, H., Burkart, J., Aliabadi, A. A., Herber, A. B., Leaitch, W. R., and Abbatt, J. P. D.: Aircraft-based measurements of High Arctic springtime aerosol show evidence for vertically varying sources, transport and composition, Atmos. Chem. Phys., 19, 57–76, https://doi.org/10.5194/acp-19-57-2019, 2019.

Winton, M.: Amplified Arctic climate change: What does surface albedo feedback have to do with it?, Geophys. Res. Lett., 33, L03 701, https://doi.org/10.1029/2005GL025244, 2006.